Four readings on Direct Searches for Dark Matter

1. "A New Search for Dark Matter 6800 feet Underground," Symmetry (August, 2017)

2. "Dark Matter Direct-Detection Experiments," Teresa Marrodán Undagoitia and Ludwig Rauch, J. Phys. G: Nucl. Part. Phys. 43 (2016) 01 3001. Sections 1, 2 and 3. Full article is on web site (but is very long!)

3. "First results from the DEAP-3600 dark matter search with argon at SNOLAB," (DEAP-3600 Collaboration) P.-A. Amaurez et al., arXiv:1707.08042v2 (2017). In particular look at Table 2 and Figure 5.

4. "First Dark Matter Search Results from the XENON1T Experiment," (XENON Collaboration) E. Aprile et al., arXiv:1705.06655v4 (2017). In particular look at Figure 2c) and see where the one candidate event lies in the S2 vs S1 plane!

symmetry
dimensions of particle physics

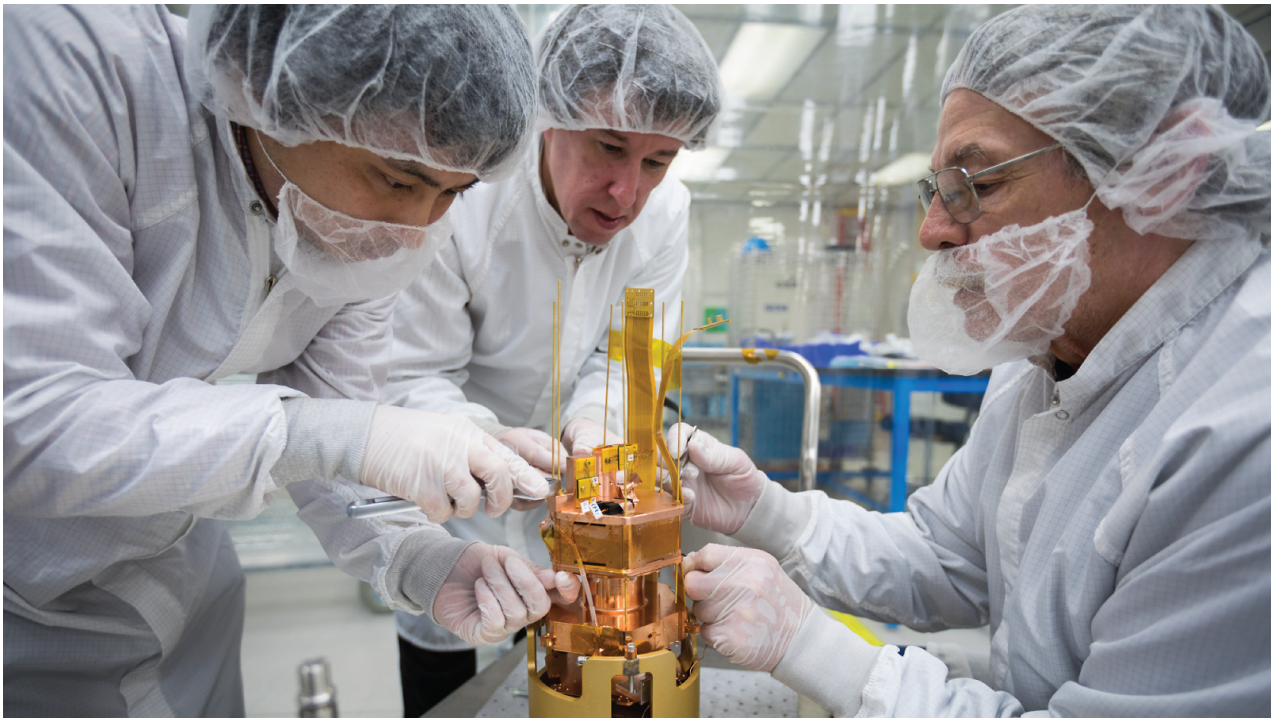

Chris Smith/SLAC National Accelerator Laboratory)

A new search for dark matter 6800 feet underground

08/08/17 | By Manuel Gnida

Prototype tests of the future SuperCDMS SNOLAB experiment are in full swing.

When an extraordinarily sensitive dark matter experiment goes online at one of the world's deepest underground research labs, the chances are better than ever that it will find evidence for particles of

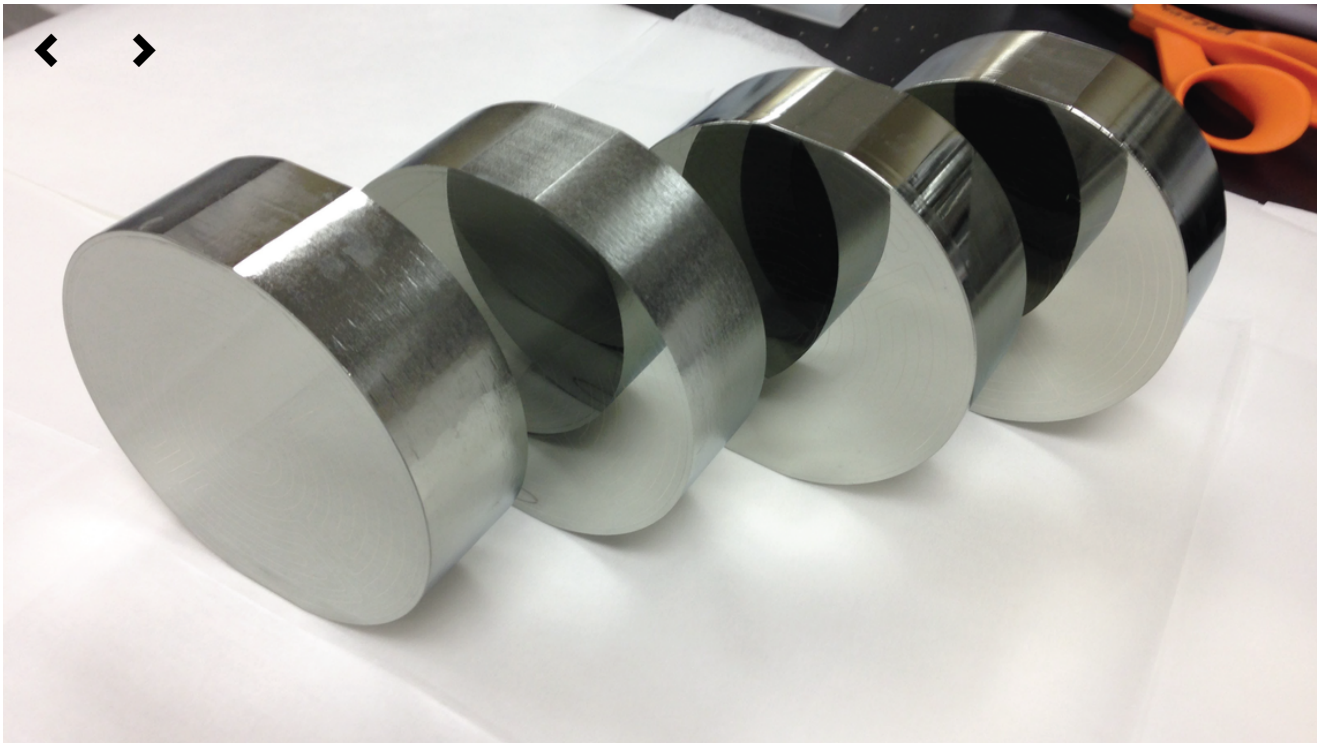

Four SuperCDMS SNOLAB iZIP detectors at the Stanford Nanofabrication Facility
Matt Cherry

dark matter—a substance that makes up 85 percent of all matter in the universe but whose constituents have never been detected.

The heart of the experiment, called SuperCDMS SNOLAB, will be one of the most sensitive detectors for hypothetical dark matter particles called WIMPs, short for "weakly interacting massive particles." SuperCDMS SNOLAB is one of two next-generation experiments (the other one being an experiment called LZ) selected by the US Department of Energy and the National Science Foundation to take the search for WIMPs to the next level, beginning in the early 2020s.

"The experiment will allow us to enter completely unexplored territory," says Richard Partridge, head of the SuperCDMS SNOLAB group at the Kavli Institute for Particle Astrophysics and Cosmology, a joint institute of Stanford University and SLAC National Accelerator Laboratory. "It'll be the world's most sensitive detector for WIMPs with relatively low mass, complementing LZ, which will look for

heavier WIMPs."

The experiment will operate deep underground at Canadian laboratory SNOLAB inside a nickel mine near the city of Sudbury, where 6800 feet of rock provide a natural shield from high-energy particles from space, called cosmic rays. This radiation would not only cause unwanted background in the detector; it would also create radioactive isotopes in the experiment's silicon and germanium sensors, making them useless for the WIMP search. That's also why the experiment will be assembled from major parts at its underground location.

A detector prototype is currently being tested at SLAC, which oversees the efforts of the SuperCDMS SNOLAB project.

Colder than the universe

The only reason we know dark matter exists is that its gravity pulls on regular matter, affecting how galaxies rotate and light propagates. But researchers believe that if WIMPs exist, they could occasionally bump into normal matter, and these collisions could be picked up by modern detectors.

SuperCDMS SNOLAB will use germanium and silicon crystals in the shape of oversized hockey pucks as sensors for these sporadic interactions. If a WIMP hits a germanium or silicon atom inside these crystals, two things will happen: The WIMP will deposit a small amount of energy, causing the crystal lattice to vibrate, and it'll create pairs of electrons and electron deficiencies that move through the crystal and alter its electrical conductivity. The experiment will measure both responses.

"Detecting the vibrations is very challenging," says KIPAC's Paul Brink, who oversees the detector fabrication at Stanford. "Even the smallest amounts of heat cause lattice vibrations that would make it

impossible to detect a WIMP signal. Therefore, we'll cool the sensors to about one hundredth of a Kelvin, which is much colder than the average temperature of the universe."

These chilly temperatures give the experiment its name: CDMS stands for "Cryogenic Dark Matter Search." (The prefix "Super" indicates that the experiment is more sensitive than previous detector generations.)

The use of extremely cold temperatures will be paired with sophisticated electronics, such as transition-edge sensors that switch from a superconducting state of zero electrical resistance to a normal-conducting state when a small amount of energy is deposited in the crystal, as well as superconducting quantum interference devices, or SQUIDs, that measure these tiny changes in resistance.

The experiment will initially have four detector towers, each holding six crystals. For each crystal material—silicon and germanium—there will be two different detector types, called high-voltage (HV) and interleaved Z-sensitive ionization phonon (iZIP) detectors. Future upgrades can further boost the experiment's sensitivity by increasing the number of towers to 31, corresponding to a total of 186 sensors.

Working hand in hand

The work under way at SLAC serves as a system test for the future SuperCDMS SNOLAB experiment. Researchers are testing the four different detector types, the way they are integrated into towers, their superconducting electrical connectors and the refrigerator unit that cools them down to a temperature of almost absolute zero.

"These tests are absolutely crucial to verify the design of these new detectors before they are integrated in the experiment underground

at SNOLAB," says Ken Fouts, project manager for SuperCDMS SNOLAB at SLAC. "They will prepare us for a critical DOE review next year, which will determine whether the project can move forward as planned." DOE is expected to cover about half of the project costs, with the other half coming from NSF and a contribution from the Canadian Foundation for Innovation.

Important work is progressing at all partner labs of the SuperCDMS SNOLAB project. Fermi National Accelerator Laboratory is responsible for the cryogenics infrastructure and the detector shielding—both will enable searching for faint WIMP signals in an environment dominated by much stronger unwanted background signals. Pacific Northwest National Laboratory will lend its expertise in understanding background noise in highly sensitive precision experiments. A number of US universities are involved in various aspects of the project, including detector fabrication, tests, data analysis and simulation.

The project also benefits from international partnerships with institutions in Canada, France, the UK and India. The Canadian partners are leading the development of the experiment's data acquisition and will provide the infrastructure at SNOLAB.

"Strong partnerships create a lot of synergy and make sure that we'll get the best scientific value out of the project," says Fermilab's Dan Bauer, spokesperson of the SuperCDMS collaboration, which consists of 109 scientists from 22 institutions, including numerous universities. "Universities have lots of creative students and principal investigators, and their talents are combined with the expertise of scientists and engineers at the national labs, who are used to successfully manage and build large projects."

SuperCDMS SNOLAB will be the fourth generation of experiments, following CDMS-I at Stanford, CDMS-II at the Soudan mine in

Minnesota, and a first version of SuperCDMS at Soudan, which completed operations in 2015.

"Over the past 20 years we've been pushing the limits of our detectors to make them more and more sensitive for our search for dark matter particles," says KIPAC's Blas Cabrera, project director of SuperCDMS SNOLAB. "Understanding what constitutes dark matter is as fundamental and important today as it was when we started, because without dark matter none of the known structures in the universe would exist—no galaxies, no solar systems, no planets and no life itself."

popular on symmetry

(/article/the-deconstructed-standard-model-equation)

07/28/16

The deconstructed Standard Model equation (/article/the-deconstructed-standard-model-equation)
The Standard Model is far more than elementary particles arranged in a table.

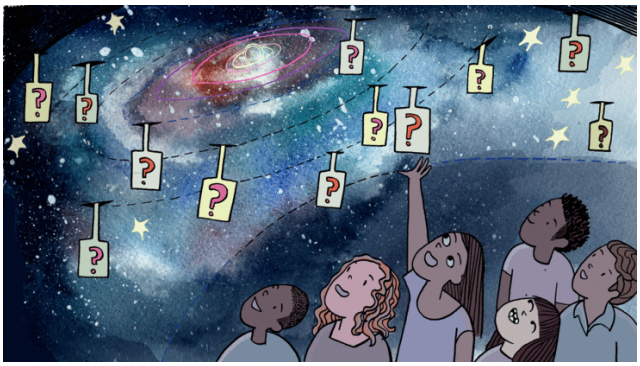

(/article/five-facts-about-the-big-bang)

08/23/16

Five facts about the Big Bang (/article/five-facts-about-the-big-bang)
It's the cornerstone of cosmology, but what is it all about?

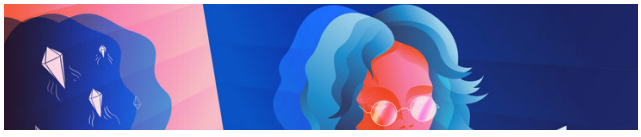

(/article/april-2015/ten-things-you-might-not-know-about-antimatter)

04/28/15

Ten things you might not know about antimatter (/article/april-2015/ten-things-you-might-not-know-about-antimatter)
Antimatter has fueled many a supernatural tale. It's also fascinating all by itself.

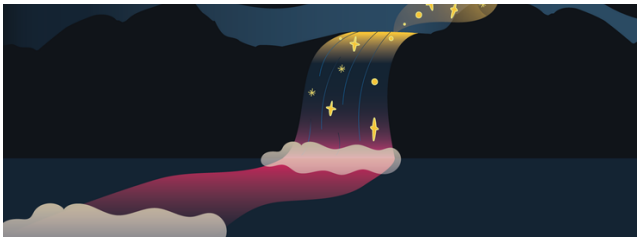

(/article/rivers-in-the-sky)

01/10/18

Rivers in the sky (/article/rivers-in-the-sky)
Local communities named newly discovered stellar streams for bodies of water close to home.

IOP Publishing Journal of Physics G: Nuclear and Particle Physics
J. Phys. G: Nucl. Part. Phys. **43** (2016) 013001 (60pp) doi:10.1088/0954-3899/43/1/013001

Topical Review

Dark matter direct-detection experiments

Teresa Marrodán Undagoitia and Ludwig Rauch

Max-Planck-Institut für Kernphysik, Saupfercheckweg 1, D-69117 Heidelberg, Germany

E-mail: marrodan@mpi-hd.mpg.de and rauch@mpi-hd.mpg.de

Received 15 September 2014, revised 26 September 2015
Accepted for publication 16 October 2015
Published 14 December 2015

Abstract

In recent decades, several detector technologies have been developed with the quest to directly detect dark matter interactions and to test one of the most important unsolved questions in modern physics. The sensitivity of these experiments has improved with a tremendous speed due to a constant development of the detectors and analysis methods, proving uniquely suited devices to solve the dark matter puzzle, as all other discovery strategies can only indirectly infer its existence. Despite the overwhelming evidence for dark matter from cosmological indications at small and large scales, clear evidence for a particle explaining these observations remains absent. This review summarises the status of direct dark matter searches, focusing on the detector technologies used to directly detect a dark matter particle producing recoil energies in the keV energy scale. The phenomenological signal expectations, main background sources, statistical treatment of data and calibration strategies are discussed.

Keywords: dark matter, dark matter searches, direct detection

(Some figures may appear in colour only in the online journal)

1. Introduction

Overwhelming evidence for gravitational interactions between baryonic and a new form of non-luminous matter can be observed on cosmological as well as astronomical scales. Its nature, however, remains uncertain. It is commonly assumed that elementary particles could be the constituents of this 'dark' matter. Such new particles, that could account for dark matter, appear in various theories beyond the standard model of particle physics. A variety of experiments have been developed over recent decades, aiming to detect these massive particles via their scattering in a detector medium. Measuring this process would provide information on the dark-matter particle mass and its interaction probability with ordinary

matter. The identification of the nature of dark matter would answer one of the most important open questions in physics and would help to better understand the Universe and its evolution. The main goal of this article is to review current and future direct-detection experimental efforts.

This review is organized in the following way. In section 2, the different phenomena indicating the existence of dark matter and possible explanations or candidates emphasizing particle solutions are presented. If, indeed, particles are the answer to the dark matter puzzle, there are three main possibilities for a verification: to produce them at particle accelerators, to look for products of e.g. their self-annihilations at locations with a high dark matter density, or to directly measure their scattering off a detector's target material. This review is dedicated to direct-detection searches for massive particles producing recoil energies in the keV energy scale. The production of dark matter particles at accelerators and searches for indirect signals are discussed only briefly. As the local density and velocity distributions of dark matter are relevant for the interpretation of the experimental results, the main characteristics of the Milky Way halo are presented in section 2. Next, in section 3, the principles of direct detection of WIMPs including the expected signal signatures are explained. Assumptions on particle and nuclear physics aspects which are necessary for the derivation of the results are summarised, and possible interpretations of the results are given. In section 4, a general overview of background sources in direct-detection experiments is given considering different types of radiation and sources of both internal and external contributions to the target material. In section 5, the basic detector technologies are introduced along with their capability to distinguish between signal and background events. Furthermore, statistical methods and the general result of an experiment are discussed. In section 6, the required calibrations to determine the energy scale, energy threshold as well as signal and background regions are detailed. In the main part of this review, section 7, the working principles of different direct detection technologies and the current experimental status are reviewed. Finally, in section 8, the experimental results are summarised, and the prospects for the future are discussed.

2. The dark matter puzzle

A wealth of observational data from gravitational effects at very different length scales supports the existence of an unknown component in our Universe. After a brief review of these observations ranging from cosmological to Milky Way-sized galaxies, various explanations and elementary-particle candidates are discussed in the following. At the end of the section, possible methods to detect particle dark matter are presented.

2.1. Dark matter indications from cosmology and astronomy

Temperature anisotropies in the cosmic microwave background (CMB), precisely measured by WMAP [1] and more recently by the Planck satellite [2], give access to the Universe when it was about 400 000 years old. The power spectrum of temperature fluctuations can be evaluated by a six-parameter model which contains, among others, the baryonic matter, dark matter and dark energy contents of the Universe. This cosmological standard model, which fits the data with high significance, is denoted Λ cold dark matter (ΛCDM) indicating that dark matter with a small random velocity is a fundamental ingredient. The Λ refers to the cosmological constant necessary to explain the current accelerated expansion of the Universe [3]. Oscillations of the baryon–photon fluid in the gravitational potential dominated by CDM density perturbations give rise to the characteristic oscillation pattern in the CMB power spectrum (acoustic peaks). From the relative height of these acoustic peaks, the amount of

baryonic matter can be estimated, which allows one to calculate the total dark matter density in the Universe. Present estimates [4] show a flat Universe with $\Omega_{\rm DM} = 0.265$, $\Omega_b = 0.049$ and $\Omega_\Lambda = 0.686$ representing the densities of dark matter, baryonic matter and dark energy, respectively.

In the standard scenario, the anisotropies of the CMB originate from quantum fluctuations during inflation. In order to understand the formation of matter distributions from the time of recombination to the present state, *N*-body simulations of dark matter particles have been carried out [5]. These simulations [6–8] propagate particles using supercomputers aiming to describe the structure growth, producing a cosmic web ranging from $\sim$10 kpc objects to the largest scales. Meanwhile, these types of simulations reproduce very accurately the measurements made by Galaxy surveys [9–11]. Measurements of the Lyman-α forest [12, 13] and weak lensing [14, 15] confirm the cosmic structure considering not only galaxies and gas clouds but also non-luminous and non-baryonic matter. Large scale simulations, which consider only dark matter, have been used to confirm theories of large scale structure formation which serve as seeds for Galaxy and cluster formation. Recently, gas and stars have been included in the simulations and it is shown that they can significantly alter the distribution of the dark matter component on small scales [16].

A further hint for the existence of dark matter arises from gravitational lensing measurements [15]. This effect discussed by Albert Einstein [17] in 1936 and later by Fritz Zwicky [18] occurs when a massive object is in the line of sight between the observer at the Earth and the object under study. The light-rays are deflected through their path due to the gravitational field resulting, for example, in multiple images or a deformation of the observable's image (strong and weak lensing, respectively). The degree of deformation can be used to reconstruct the gravitational potential of the object that deflects the light along the line of sight. From various observations it has been found that the reconstructed mass using this method is greater than the luminous matter, resulting in very large mass to light ratios (from a few to hundreds). Gravitational lensing has also been applied in Galaxy-cluster collisions to reconstruct the mass distributions in such events where mass to light ratios of $>$200 are measured. In some examples [19–21] and in an extensive study of 72 cluster collisions [22], the reconstructed gravitational centers appear clearly separated from the main constituent of the ordinary matter, i.e. the gas clouds which collide and produce detectable x-rays. This can be interpreted as being due to dark matter haloes that continue their trajectories independently of the collision. An upper limit to the self-interaction cross-section for dark matter can be derived from these observations [23].

Indications for non-luminous matter appear in our Universe also at smaller scales. Historically, the first indications for dark matter arose from astronomical observations. In order to explain measurements of the dynamics of stars in our Galaxy, the word 'dark matter' was already used by Kapteyn [24] in 1922 but it was not the correct physical explanation of the observed phenomenon. The first evidence of dark matter in the present understanding was the measurement of unexpectedly high velocities of nebulae in the Coma cluster which brought Zwicky [25] to the idea that a large amount of dark matter could be the explanation for the unexpected high velocities. In 1978, Rubin *et al* [26] found that rotation velocities of stars in galaxies stay approximately constant with increasing distance to their galactic center. This observation was in contradiction with expectation, as objects outside the visible mass distribution should have velocities $v \propto 1/\sqrt{r}$ following Newtonian dynamics. A uniformly distributed halo of dark matter could explain both the velocities in clusters and the rotation velocities of objects far from the luminous matter in galaxies (e.g. [27]).

2.2. The nature of dark matter: possible explanations and candidates

A plausible solution to describe some of the astronomical measurements mentioned in section 2.1 is a modification of gravitation laws to accommodate the observations. Such modified Newtonian dynamic models like MOND [28] or its relativistic extension TeVeS [29] can, for instance, successfully describe rotational velocities measured in galaxies. However, MOND fails or needs unrealistic parameters to fit observations on larger scales such as structure formation or the CMB structure and violates fundamental laws such as momentum conservation and the cosmological principle [30]. While TeVeS can solve some of the conceptual problems of MOND, the required parameters seem to generate an unstable Universe [31] or fail to simultaneously fit lensing and rotation curves [32].

Massive astrophysical compact halo objects (MACHOs) have also been considered as a possible explanation for the large mass to light ratios detected in the astronomical observations described in the previous section. These objects could be neutron stars, black holes, brown dwarfs or unassociated planets that would emit very little to no radiation. Searches for such objects using gravitational microlensing [33] towards the Large Magellanic Cloud have been performed [34]. Extrapolations to the Galactic dark matter halo showed that MACHOs can make up about 20% of the dark matter in our Galaxy and that a model with MACHOs accounting entirely for the dark-matter halo is ruled out at 95% confidence level [34]. The baryonic nature of dark matter is actually also ruled out by big-bang nucleosynthesis (BBN). The abundance of light elements predicted by BBN depends on the baryon density and, in fact, measurements constrain the baryon density to a value around $\Omega_b = 0.04$ [35] close to the value derived from CMB.

A more common ansatz is to assume that dark matter is made out of massive neutral particles featuring a weak self-interaction. From the known particles in the standard model, only the neutrino could be considered. Due to its relativistic velocity in the early Universe, the neutrino would constitute a hot dark matter candidate. Cosmological simulations have shown, however, that a Universe dominated by neutrinos would not be in agreement with the observed clustering scale of galaxies [36]. Furthermore, due to the fermionic character of neutrinos, their occupation number is constrained by the Fermi–Boltzmann distribution, so they cannot account for the observed dark-matter density in halos [37]. Sterile neutrinos are hypothetical particles which were originally introduced to explain the smallness of the neutrino masses [38]. Additionally, they provide a viable dark matter candidate. Depending on their production mechanism, they would constitute a cold (non-relativistic at all times) or a warm (relativistic only in an early epoch) dark matter candidate [39, 40]. Possible masses, which are not yet constrained by x-ray measurements or the analysis of dwarf spheroidal galaxies, range from 1 keV to tens of keV. Given this very low mass, and the low interaction strength, the existence of sterile neutrinos is not tested by direct detection experiments. An indication could, for example, arise from the x-ray measurement of the sterile neutrino decay via the radiative channel $N \rightarrow \nu\gamma$ [41].

Models beyond the standard model of particle physics suggest the existence of new particles which could account for the dark matter. If such hypothetical particles were stable, neutral and had a mass from below GeV$/c^2$ to several TeV$/c^2$, they could be the weakly interacting massive particles (WIMPs). The standard production mechanism for WIMPs assumes that in the early Universe these particles were in equilibrium with the thermal plasma [42]. As the Universe expanded, the temperature of the plasma became lower than the WIMP mass resulting in the decoupling from the plasma. At this freeze-out temperature, when the WIMP annihilation rate was smaller than the Hubble expansion rate, the dark matter relic density was reached. The cross-section necessary to observe the current dark matter density is

of the order of the weak interaction scale. It appears as a great coincidence that a particle interacting via the weak force would produce the right relic abundance and, therefore, the WIMP is a theoretically well motivated dark matter candidate.

Supersymmetry models [43] are proposed as extensions of the standard model of particle physics to solve the hierarchy problem as well as the unification of weak, strong and electromagnetic interactions. In this model, a whole new set of particles are postulated such that for each particle in the standard model there is a supersymmetric partner. Each particle differs from its partner by $1/2$ in spin and, consequently, bosons are related to fermions and vice versa. The neutralino, the lightest neutral particle which appears as a superposition of the partners of the standard model bosons, constitutes an example of a new particle fulfilling the properties of a WIMP. The typical masses predicted for the neutralino range from few GeV/c^2 to several TeV/c^2. A WIMP candidate appears also in models with extra–dimensions. In such models N spatial dimensions are added to the $(3 + 1)$ space–time classical ones. They appeared already around 1920 to unify electromagnetism with gravity. The lightest stable particle is called 'lightest Kaluza particle' and constitutes also a good WIMP candidate [44, 45].

Among the non-WIMP candidates, 'superheavy dark matter' or 'WIMPzillas' are postulated to explain the origin of ultra high-energy cosmic rays [46]. At energies close to 10^{20} eV, cosmic protons can interact with the CMB and, thus, their mean free path is reduced resulting in a suppressed measured flux [47, 48]. Experimental results include, however, the detection of a few events above the expected cut-off, motivating a superheavy dark matter candidate. Decays of these non-thermally produced [49] superheavy particles with masses of $(10^{12} - 10^{16})\,\mathrm{GeV}/c^2$ could account for the observations, being at the same time responsible for the dark matter in the Universe.

Finally, a very well motivated particle and dark matter candidate is the axion. In the standard model of particle physics, there is no fundamental reason why QCD should conserve P and CP. However, from the experimental bound on the neutron electric dipole moment [50], very small values of P and CP violation can be derived. In order to solve this so-called 'strong CP-problem' [51], a new symmetry was postulated [52] in 1977. When this symmetry is spontaneously broken, a massive particle, the axion, appears. The axion mass and the coupling strength to ordinary matter are inversely proportional to the breaking scale which was originally associated to the electroweak scale. This original axion model is ruled out by laboratory experiments [53]. Cosmological and astrophysical results also provide very strong bounds on the axion hypothesis [51]. There exist, however, further 'invisible' axion models in which the breaking scale is a free parameter, KSVZ [54, 55] and DFSZ [56, 57], and still provide a solution to the CP-problem. Invisible axions or axion-like particles, would have been produced non-thermally in the early Universe by mechanisms like the vacuum realignment [58, 59] for example, giving the right dark matter abundance. The resulting free streaming length would be small and, therefore, these axions are a 'cold' candidate. For certain parameters, axions could account for the complete missing matter [60].

Sterile neutrinos, WIMPs, superheavy particles and axions are not the only particle candidates proposed. The candidates mentioned above arise from models that were proposed originally with a different motivation and not to explain dark matter. The fact that the models are motivated by different unresolved observations strengthen the relevance of the predicted dark matter candidate. A more comprehensive review on dark matter candidates can be found for example in [61]. This article focuses on the direct detection of WIMPs and just some brief information on searches for particles that would induce an electronic recoil (e.g. axion-like particles) will be given in the following.

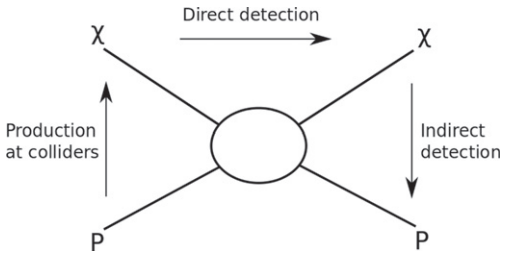

Figure 1. Schematic showing the possible dark matter detection channels.

2.3. Searches for dark matter particles

The particle dark matter hypothesis can be tested via three processes: the production at particle accelerators, indirectly by searching for signals from annihilation products, or directly via scattering on target nuclei. Figure 1 shows a schematic representation of the possible dark matter couplings to a particle, P, of ordinary matter.

While the annihilation of dark matter particles (downwards direction) could give pairs of standard model particles, the collision of electrons or protons at colliders could produce pairs of dark matter particles. In this section the production and indirect detection methods as well as the current status of searches are briefly summarised. The subsequent sections and main part of this review are then devoted to the direct detection of dark matter, $\chi \mathrm{P} \rightarrow \chi \mathrm{P}$ (horizontal direction in figure 1).

Since the start of the Large Hadron Collider (LHC) at CERN in 2008, the CMS [62] and ATLAS [63] experiments have searched for new particles in proton–proton collisions at a center-of-mass energy of 7 TeV. Besides the discovery of the Higgs particle [64, 65], CMS and ATLAS have studied a number of new particle signatures by scanning the parameter space of different supersymmetric and extra-dimensions models. The presence of a dark matter particle would only be inferred by observing events with missing transferred momentum and energy. Therefore, events with, e.g., an energetic jet and an imbalanced momentum transfer are selected for analysis. Reactions of the type

$$pp \rightarrow \chi\overline{\chi} + x \tag{1}$$

are probed, x being a hadronic jet, a photon or a leptonically decaying Z or W boson. The results obtained so far are consistent with the standard model expectations (see for example [66–68]) but further searches will be performed in the next few years for higher center-of-mass energy. The derived bounds can be translated into limits on the cross-section for a given particle mass. Bounds arising from accelerator searches are most constraining below $\sim$4 GeV and $\sim$700 GeV for spin-independent (SI) and spin-dependent (SD) (proton coupling, see section 3.2) interactions, respectively [66]. However, a direct comparison of these experimental results to other detection methods is, in general, model dependent (see the discussion in section 8).

Dark matter particles can gravitationally accumulate in astrophysical objects such as stars, galaxies or our Sun. The most favoured sources to search for indirect signals are the galactic centre and halo, close Galaxy clusters or dwarf galaxies also called dwarf spheroidals. The latter are very popular locations due to their large measured mass to light ratio and their small background. Due to the increased dark-matter density, an enhanced self-annihilation, scattering or decay into standard model particles could produce a measurable particle flux (see [69] for a detailed discussion). The measurement of these secondary particles is a further

detection mechanism usually denoted as 'indirect detection'. Examples of possible annihilation channels are

$$\chi\overline{\chi} \rightarrow \gamma\gamma,\ \gamma Z,\ \gamma H \quad \text{or} \tag{2}$$

$$\chi\overline{\chi} \rightarrow q\bar{q},\ W^{-}W^{+},\ ZZ. \tag{3}$$

Some of the products decay further into $e^{-}e^{+}$, $p\overline{p}$,γ-rays and neutrinos. A second mechanism to generate charged (anti-) particles, photons or neutrinos from dark matter is given by its decay. In contrast to self-annihilation processes, where the production rate shows a quadratic dependence of the dark matter density, decaying dark matter scales only linearly (e.g. [70]). In addition, dark matter particles might be gravitationally captured inside the Sun due to the elastic scattering with its nuclei. The annihilation of captured dark-matter particles can produce neutrinos which can propagate out of the Sun and might be detectable with Earth-based neutrino telescopes. Note that the total number of captured particles is less affected by uncertainties of the dark matter halo since this process lasts for billions of years and dark matter density variations are averaged out [70].

Produced charged particles are deflected in the interstellar magnetic fields, losing the information on their origin. Due to their charge neutrality, γ-rays and neutrinos point, instead, to the source where they were produced. While neutrinos travel unaffected from the production source, γ-rays can be affected by absorption in the interstellar medium.

Imaging atmospheric Cherenkov telescopes for TeV γ-ray detection can look specifically in the direction of objects where a large amount of dark matter is expected. Either a γ-flux in dwarf galaxies or Galaxy clusters, or mono-energetic line signatures are searched for. So far no significant signal from dark matter annihilations has been observed, and upper limits are derived by the MAGIC [71, 72], HESS [73, 74] and VERITAS [75, 76] telescopes. Indirect searches can be also performed by satellite-based instruments capable of detecting low-energy γ-rays (approx. 20 MeV–300 GeV) like Fermi-LAT [77]. Although some gamma-ray features identified in the Fermi data are intriguing (for example [78–80]), in the publication of early 2015 by the Fermi collaboration [81] no evidence for a dark-matter signal is found. One of the strongest and most robust constraints can be derived by the Fermi-LAT observation of dwarf spheroidal satellite galaxies of the Milky Way as those are some of the most dark-matter-dominated objects known [82]. Consequently, conservative limits on the annihilation cross-section of dark matter particles ranging from a few GeV to a few tens of TeV are derived. In the energy region of (0.1–10) keV, x-ray satellites such as XMM-Newton and Chandra provide data to search for indirect dark matter signals. In 2014, an unexpected line at 3.5 keV was found in the data recorded by both satellites [83, 84]. This signal can be interpreted by a decay of dark matter candidates, for instance, from sterile neutrinos or axions [85–88]. Other astrophysical explanations have been, however, proposed and thus, the origin of the signal remains controversial (see e.g. [89–91]). Large neutrino detectors like Ice Cube or Super-Kamiokande are able to search for dark matter annihilations into neutrinos. No evidence for such a signal has been observed, resulting in constraints on the cross-section [92, 93]. Finally, also charged particles like protons, antiprotons, electrons and positrons can be detected by satellites. Measurements on the steadily increasing positron fraction from 10 to $\sim$250 GeV by Pamela [94] and AMS [95] raise discussions on its possible dark matter origin. However, given that such a spectrum could be also described by astrophysical objects like pulsars (rapidly rotating neutron stars) or by the secondary production of e^{+} by the collision of cosmic rays with interstellar matter [96], this cannot be considered as a clear indication of a dark matter signal.

3. Principles of WIMP direct detection

Large efforts have been pursued to develop experiments which are able to directly test the particle nature of dark matter. The aim is to identify nuclear recoils produced by the collisions between the new particles and a detector's target nuclei. The elastic scattering of WIMPs with masses of (10–1000) GeV$/c^2$ would produce nuclear recoils in the range of (1–100) keV [97]. To unambiguously identify such low-energy interactions, a detailed knowledge on the signal signatures, the particle physics aspects and nuclear physics modelling is mandatory. Furthermore, for the calculation of event rates in direct-detection experiments, the dark matter density and the halo velocity distribution in the Milky Way are required. This section is devoted to reviewing all these aspects, focusing on WIMP dark matter, whereas non-WIMP candidates are briefly discussed in section 3.3.

3.1. Experimental signatures of dark matter

The signature of dark matter in a direct-detection experiment consists of a recoil spectrum of single-scattering events. Given the low interaction strength expected for the dark matter particle, the probability of multiple collisions within a detector is negligible. In the case of a WIMP, a nuclear recoil is expected [98]. The differential recoil spectrum resulting from dark matter interactions can be written, following [97], as:

$$\frac{\mathrm{d}R}{\mathrm{d}E}(E,\,t) = \frac{\rho_0}{m_\chi \cdot m_A} \cdot \int v \cdot f(\mathbf{v},\,t) \cdot \frac{\mathrm{d}\sigma}{\mathrm{d}E}(E,\,v)\,\mathrm{d}^3v, \tag{4}$$

where m_χ is the dark matter mass and $\frac{\mathrm{d}\sigma}{\mathrm{d}E}(E,\,v)$ its differential cross-section. The WIMP cross-section σ and m_χ are the two observables of a dark matter experiment. The dark matter velocity v is defined in the rest frame of the detector and m_A is the nucleus mass. Equation (4) shows explicitly the astrophysical parameters, the local dark matter density ρ_0 and $f(\mathbf{v},\,t)$, which accounts for the WIMP velocity distribution in the detector reference frame. This velocity distribution is time dependent due to the revolution of the Earth around the Sun. Based on equation (4), detection strategies can exploit the energy, time or direction dependences of the signal.

The most common approach in direct-detection experiments is the attempt to measure the energy dependence of dark matter interactions. According to [97], equation (4) can be approximated by

$$\frac{\mathrm{d}R}{\mathrm{d}E}(E) \approx \left(\frac{\mathrm{d}R}{\mathrm{d}E}\right)_0 F^2(E)\exp\left(-\frac{E}{E_\mathrm{c}}\right), \tag{5}$$

where $\left(\frac{\mathrm{d}R}{\mathrm{d}E}\right)_0$ denotes the event rate at zero momentum transfer and E_c is a constant parameterizing a characteristic energy scale which depends on the dark matter mass and target nucleus [97]. Hence, the signal is dominated at low recoil energies by the exponential function. $F^2(E)$ is the form-factor correction which will be described in more detail in section 3.2.

Another possible dark matter signature is the so-called 'annual modulation'. As a consequence of the Earth rotation around the Sun, the speed of the dark matter particles in the Milky Way halo relative to the Earth is largest around 2 June and smallest in December. Consequently, the amount of particles able to produce nuclear recoils above the detectors' energy threshold is also largest in June [99]. As the amplitude of the variation is expected to be small, the temporal variation of the differential event rate can be written, following [100], as

$$\frac{\mathrm{d}R}{\mathrm{d}E}(E,\,t) \approx S_0(E) + S_m(E) \cdot \cos\left(\frac{2\pi\,(t - t_0)}{T}\right), \tag{6}$$

where t_0 is the phase which is expected at about 150 d and T is the expected period of one year. The time-averaged event rate is denoted by S_0, whereas the modulation amplitude is given by S_m. A rate modulation would, in principle, enhance the ability to discriminate against background and help to confirm a dark matter detection.

Directionality is another dark matter signature which can be employed for detection as the direction of the nuclear recoils resulting from WIMP interactions has a strong angular dependence [101]. This dependence can be seen in the differential rate equation when it is explicitly written as a function of the angle γ, defined by the direction of the nuclear recoil relative to the mean direction of the solar motion

$$\frac{\mathrm{d}R}{\mathrm{d}E\ \mathrm{d}\cos\gamma} \propto \exp\left[\frac{-\left[\,(v_\mathrm{E} + v_\odot)\cos\,\gamma - v_\mathrm{min}\right]^2}{v_\mathrm{c}^2}\right]. \tag{7}$$

In equation (7), v_E represents the Earth's motion, $v_\odot$ the velocity of the Sun around the Galactic centre, v_min the minimum WIMP velocity that can produce a nuclear recoil of an energy E and v_c the halo circular velocity $v_\mathrm{c} = \sqrt{3/2}\,v_\odot$. The integrated rate of events scattering in the forward direction will, therefore, exceed the rate for backwards scattering events by an order of magnitude [101]. An oscillation of the mean direction of recoils over a sidereal day is also expected due to the rotation of the Earth and if the detector is placed at an appropriate latitude. This directional signature allows one to discriminate potential backgrounds [102]. A detector able to determine the direction of the WIMP-induced nuclear recoil would provide a powerful tool to confirm the measurement of dark matter particles. Such directional searches are summarized in section 7.6.

3.2. Cross-sections and nuclear physics aspects

To interpret the data of dark matter experiments, further assumptions on the specific particle-physics model as well as on the involved nuclear-physics processes have to be made. This section summarises the most common interactions between dark matter particles and the target nucleons.

For WIMP interactions that are independent of spin, it is assumed that neutrons and protons contribute equally to the scattering process (isospin conservation). For sufficiently low momentum transfer q, the scattering amplitudes of each nucleon add in phase and result in a coherent process. For SD interactions, only unpaired nucleons contribute to the scattering. Therefore, only nuclei with an odd number of protons or neutrons are sensitive to these interactions. In this case, the cross-section is related to the quark spin content of the nucleon with components from both proton and neutron couplings.

When the momentum transfer is such that the particle wavelength is no longer large compared to the nuclear radius, the cross-section decreases with increasing q. The form factor F accounts for this effect and the cross-section can be expressed as: $\sigma \propto \sigma_0 \cdot F^2$, where σ_0 is the cross-section at zero momentum transfer. In general, the differential WIMP–nucleus cross section, $\mathrm{d}\sigma/\mathrm{d}E$ shown in equation (4), can be written as the sum of an SI contribution and an SD one

$$\frac{\mathrm{d}\sigma}{\mathrm{d}E} = \frac{m_A}{2\mu_A^2 v^2} \cdot \left(\sigma_0^\mathrm{SI} \cdot F_\mathrm{SI}^2(E) + \sigma_0^\mathrm{SD} \cdot F_\mathrm{SD}^2(E)\right). \tag{8}$$

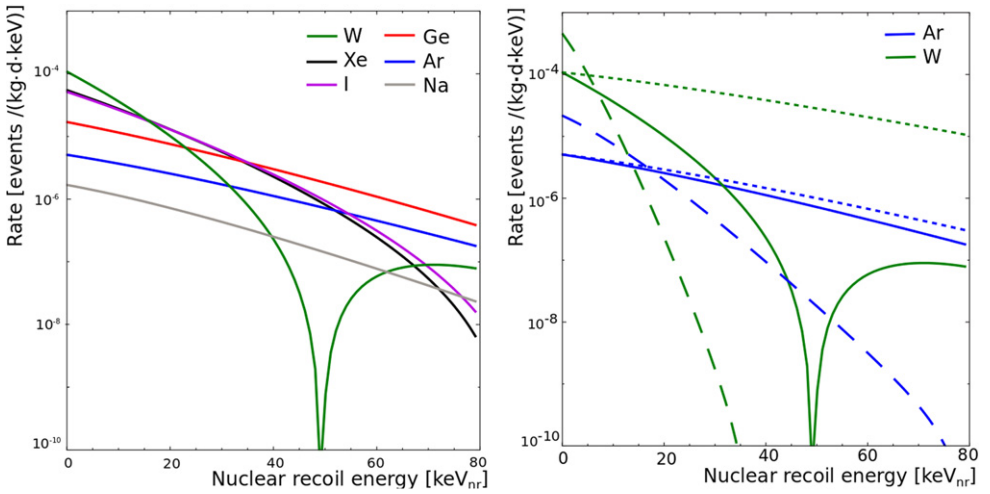

Figure 2. (Left) Differential event rate for the direct detection of a 100 GeV/c^2 WIMP with a cross-section of 10^{-45} cm^2 in experiments using tungsten (green), xenon (black), iodine (magenta), germanium (red), argon (blue) and sodium (grey) as target materials. (Right) The event rate is shown for a heavy and a light target as indicated in green (tungsten) and blue (argon), respectively, showing the effect of neglecting the form factor correction (dotted line) and the effect of a lower WIMP mass of 25 GeVc^2 (dashed line).

The WIMP–nucleus reduced mass is described by μ_A. For SI interactions, the cross-section at zero momentum transfer can be expressed as

$$\sigma_0^{\mathrm{SI}} = \sigma_{\mathrm{p}} \cdot \frac{\mu_A^2}{\mu_{\mathrm{p}}^2} \cdot \left[Z \cdot f^{\mathrm{p}} + (A - Z) \cdot f^{\mathrm{n}} \right]^2 \tag{9}$$

where $f^{\mathrm{p,n}}$ are the contributions of protons and neutrons to the total coupling strength, respectively, and μ_{p} is the WIMP–nucleon reduced mass. Usually, $f^{\mathrm{p}} = f^{\mathrm{n}}$ is assumed and the dependence of the cross-section with the number of nucleons A takes an A^2 form. The form factor for SI interactions is calculated assuming the distribution of scattering centres to be the same as the charge distribution derived from electron scattering experiments [97]. Commonly, the Helm parameterization [103] is used to describe the form factor. Recent shell-model calculations [104] show that the derived structure factors are in good agreement with the classical parameterization.

To visualize the effect of the target isotope and the form-factor correction, figure 2 (left) shows the event rate given in number of events per keV, day and kg (equation (4)) for SI interactions in different target materials: tungsten in green, xenon in black, iodine in magenta, germanium in red, argon in blue and sodium in grey. A WIMP mass of 100 GeV/c^2 and a cross-section of 10^{-45} cm^2 are assumed for the calculation. In these curves both the A^2 dependence of the cross-section and the form-factor correction affect the shape of the energy spectrum. Heavier elements profit from the A^2 enhancement with a higher event rate at low deposited energies but the coherence loss due to the form factor suppresses the event rate especially at higher recoil energies. Therefore, for lighter targets a low energy threshold is of less relevance than for the heavier ones. Figure 2 (right) shows separately the WIMP mass and the form-factor effect on the differential event rate without considering the nuclear recoil acceptance and the energy threshold of the detector. Solid lines show the expected rates for a

$100\,\mathrm{GeV}/c^2$ WIMP as in the left figure for a heavy and a light target as indicated in green (tungsten) and blue (argon), respectively. In comparison to the heavy WIMP mass the rates for a $25\,\mathrm{GeV}/c^2$ dark matter particle (dashed line) drop steeper as the momentum transfer is smaller. The form factor correction for a heavy target is more important than for light targets. This can be seen by the dotted lines representing rates for a $100\,\mathrm{GeV}/c^2$ WIMP, calculated without the form-factor correction.

For SD interactions, the form factor is written in terms of the spin structure function whose terms are determined from nuclear shell model calculations [105, 106]. A common practice is to express the cross-section for the interaction with protons and with neutrons

$$\sigma_0^{\mathrm{SD}} = \frac{32}{\pi}\mu_A^2 \cdot G_{\mathrm{F}}^2 \cdot \left[a_{\mathrm{p}} \cdot \left\langle S^{\mathrm{p}} \right\rangle + a_n \cdot \left\langle S^{\mathrm{n}} \right\rangle\right]^2 \cdot \frac{J+1}{J}, \tag{10}$$

where G_{F}^2 is the Fermi coupling constant, J the total nuclear spin and $a_{\mathrm{p,n}}$ the effective proton (neutron) couplings. The expectation value of the nuclear spin content due to the proton (neutron) group is denoted by $\langle S^{\mathrm{p,n}} \rangle$. New calculations performed in [107] use chiral effective-field theory (EFT) currents to determine the couplings of WIMPs to nucleons up to the leading two-nucleon currents. This method yields an improved agreement between the calculated and measured energy spectra of the considered nuclei as well as the ordering of the nuclear levels (e.g. [108]). These calculations have been used to calculate the couplings for the most relevant isotopes in direct detection experiments: ^{129,131}Xe, ^{127}I, ^{73}Ge, ^{19}F, ^{23}Na, ^{27}Al and ^{29}Si.

In the context of a non-relativistic EFT for WIMP-like interactions, a more detailed formulation of possible couplings from dark matter to baryons has been proposed [109–111] and is applied by some experiments [112]. Instead of the classical two (SI and SD) couplings, six possible nuclear response-functions are assumed which are described by 14 different operators. In this model, the nucleus is not treated as a point-like particle; instead, its composite nature is reflected. Thus, the spin response function is split in transverse and longitudinal components and new response functions arise from the intrinsic velocities of the nucleons. Note that the form factor F, as introduced above, tries to account for the finite spatial extend of the nuclear charge and spin densities. This correction, however, is only approximate. The EFT operators are constructed by four three-vectors $i\frac{\vec{q}}{m_{\mathrm{N}}}$, $\vec{v}^{\perp}$, $\vec{S}_{\mathrm{N}}$, $\vec{S}_{\chi}$ which describe the momentum transfer q scaled with the nucleon mass m_{N}, the WIMP–nucleon relative velocity $\vec{v}^{\perp}$, the spin of the nucleus $\vec{S}_{\mathrm{N}}$ and the possible spin of the dark matter particle $\vec{S}_{\chi}$, respectively. The standard SI (equation (9)) and SD (equation (10)) interactions are described by operators $\mathcal{O}_1$ and $\mathcal{O}_4$ with 1 being the identity matrix

$$\mathcal{O}_1 = 1_{\chi}\,1_{\mathrm{N}},\ \mathcal{O}_4 = \vec{S_{\chi}} \cdot \vec{S_{\mathrm{N}}}. \tag{11}$$

The SI interactions are, furthermore, decomposed into two longitudinal components and a transversal spin component, as in general interactions do not couple to all spin projections symmetrically. New operators arise also by a direct velocity dependence. The impact of the detailed EFT approach on the dark matter limits in comparison to the conventional SI/SD interaction has been calculated in [112] and shows that, in some cases, the compatibility of results among experiments using different targets is significantly affected. Furthermore, destructive interference effects among operators can weaken standard direct-detection exclusion limits by up to one order of magnitude in the coupling constants [113]. This approach not only generalizes the traditional SI and SD parameter space but also allows one to constrain, in an easier way, dark matter models due to the variety of constrained operators.

3.3. Other interpretations

The previous section describes a model where dark matter particles scatter off the target nucleus producing nuclear recoils; however, various other models exist. This section briefly summarises a selection of alternative dark matter interactions for which experiments have derived results.

An extension of the standard elastic scattering off nuclei is an inelastic scattering off the WIMP, which was motivated to solve discrepancies among experimental results [114]. In this approach, WIMPs are assumed to only scatter off nuclei by simultaneously getting excited to a higher state with an energy δ above the ground state. The elastic scattering would be, in this case, highly suppressed or even forbidden. The energy spectrum is suppressed at low energies due to the velocity threshold for the inelastic scattering process. Experimental constraints on this model have been shown e.g. in [115–117]. Another possibility is the inelastic WIMP–nucleus scattering in which the target nucleus is left in a low-lying nuclear excited state [118]. The signal would have a signature of a nuclear recoil followed by a γ-ray from the prompt de-excitation of the nucleus. As an example, the inelastic structure functions have been calculated for xenon in [119] and are used in [120] to derive the corresponding exclusion limits for this process.

In contrast to interactions with nucleons, various models allow a dark matter scattering off electrons. For instance, sub-GeV dark matter particles could produce detectable ionization signals [121] and, indeed, limits have been derived for such candidates [122]. Furthermore, if new forms of couplings are introduced to mediate the dark matter–electron interactions, further models become viable. By assuming an axial-vector coupling [123], the dark matter–lepton interactions dominate at tree level and cannot be probed by dark matter–baryon scattering. Furthermore, models such as kinematic-mixed mirror dark matter [124] or luminous dark matter [125] also predict interactions with atomic electrons.

New couplings are also introduced to mediate interactions of axion-like particles (ALPs) with electrons via the axioelectric (also photoelectric-like) or Primakov processes [126] (see section 2.2). These processes, invoked by sufficiently massive particles in direct detection experiments, involve only the emission of electrons and x-rays and therefore cannot be separated from the experimental electronic recoil background. Nevertheless, bounds on these models have been derived from data of various experiments [127–130]. The same interactions are assumed for bosonic super-weakly interacting massive dark matter candidates [131] but their electronic recoil energy scale is in general higher and limits are derived in [132].

3.4. Distribution of dark matter in the Milky Way

The dark matter density in the Milky way at the position of the Earth and its velocity distribution are astrophysical input parameters, needed to interpret the results of direct-detection experiments. In this section, the parameters of the standard halo model typically used to derive the properties of dark matter interactions, their uncertainties and the differences in modelling the dark-matter halo itself are summarised.

It is common to assume a local dark matter density of 0.3 GeV cm^{-3} which results from mass modelling of the Milky Way, using parameters in agreement with observational data [133]. However, depending on the profile model used for the halo, a density range from (0.2–0.6) GeV cm^{-3} can be derived (see [134] for a review on this topic).

The dark matter velocity profile is commonly described by an isotropic Maxwell–Boltzmann distribution

$$f(\mathbf{v}) = \frac{1}{\sqrt{2\pi\sigma}} \cdot \exp\left(-\frac{|\mathbf{v}|^2}{2\sigma^2}\right) \tag{12}$$

which is truncated at velocities exceeding the escape velocity. Here, the dispersion velocity σ is related to the circular velocity via $\sigma = \sqrt{3/2}\ v_c$. A standard value of $v_c = 220\,\mathrm{km\,s^{-1}}$ is used for the local circular speed. This value results from an average of values found in different analyses [135]. More recent studies using additional data and/or different methods, find velocities ranging from $(200 \pm 20)\,\mathrm{km\,s^{-1}}$ to $(279 \pm 33)\,\mathrm{km\,s^{-1}}$ [133]. Finally, the escape velocity defines a cut-off in the description of the standard halo profile. The commonly used value of $544\,\mathrm{km\,s^{-1}}$ is the likelihood median calculated using data from the RAVE survey [136]. The 90% confidence interval contains velocities from $498\,\mathrm{km\,s^{-1}}$ to $608\,\mathrm{km\,s^{-1}}$. These large ranges of possible values for the dark matter density, circular speed and escape velocity illustrate that the uncertainties in the halo modelling are significant. The GAIA satellite[1], in orbit since January 2014, has been designed to measure about a billion stars in our Galaxy and throughout the Local Group. These unprecedented positional and radial velocity measurements will reduce the uncertainties on the local halo model of the Milky Way.

Not only do the parameters of the dark matter halo show uncertainties but also modelling the halo itself inherits strong assumptions. A sharp truncation of the assumed Maxwell–Boltzmann distribution at the escape velocity has to be unphysical, which motivated the idea of King models (e.g. [137, 138]) trying to account naturally for the finite size of the dark matter halo. It is also possible that the velocity distribution is anisotropic, giving rise to triaxial models, allowing different velocities in each dimension of the velocity vector (e.g. [139, 140]). If the dark matter halo is not virialized, it could give rise to local inhomogeneities, e.g. subhalos, tidal streams or unbound dark matter particles with velocities exceeding the escape velocity. It is worth mentioning that the effect of these assumptions on the astrophysical parameters and dark matter halo distributions on the results of different experiments is reduced by choosing the common values as introduced above. However, the effects can also be energy dependent, thus altering the detector response for diverse target materials. Therefore, other analysis methods are necessary to resolve these ambiguities (see section 5).

The dark matter density profile can only be indirectly observed (e.g. rotation velocities of stars); therefore, numerical simulations have been performed in order to understand the structure of halos. These simulations contained traditionally only dark matter [141–144] and showed triaxial velocity distributions [140]. The resulting haloes feature, however, cusped profiles with steeper density variations towards the centre of the halo, while observations favoured flatter cored-profiles. Moreover, the simulations predict a large amount of substructure, i.e. large number of subhaloes, in contradiction with the few haloes present in the Milky Way. These issues, currently under investigation, might challenge the validity of the ΛCDM model and different possible solutions are discussed. One solution could be related to the nature of dark matter or its properties [145]. A warm dark matter candidate with a larger free-streaming length could, for instance, modify the halo density profile resulting in the observed cored-type profiles and suppressing the formation of small structure. Another possibility is to consider candidates with weak interaction with matter but strong self-interaction [146]. The elastic scattering of these particles in the dense central region could modify the energy and momentum distribution resulting in cored dark matter profiles. Probably, the solution could be related to the absence of baryonic matter in the simulations. The effect of

[1] http://sci.esa.int/gaia

baryons to the halo mass distribution is observed, for instance, in the recent Illustris-1 simulation [8] which considers the coevolution of both dark and visible matter in the Universe. Furthermore, sudden mass outflows can alter substantially the central structure of haloes [147]. Dark matter simulations including also baryons [16] show how gas outflows can change the distribution of gas and stars. For sufficiently fast outflows, the dark matter distribution can be also affected explaining hereby the low central-halo densities.

Nevertheless even with large simulations containing baryons, uncertainties in the dark matter halo remain and, thus, direct-detection experiments generally use the common assumption of an isotropic Maxwell–Boltzmann distribution using values for astrophysical parameters as introduced above. In section 5.3, a method to display results in an astrophysical independent representation is described.

4. Background sources and reduction techniques

In order to identify unambiguously interactions from dark matter particles, ultra-low background experimental conditions are required. This section summarises the various background contributions for a direct dark matter experiment. It includes external radiation by γ-rays, neutrons and neutrinos which is common for all experiments and internal backgrounds for solid-state and for liquid detectors. The main strategies to suppress these backgrounds through shielding, material selection, and reduction in data analysis are also discussed.

4.1. Environmental gamma-ray radiation

The dominant radiation from gamma-decays originates from the decays in the natural uranium and thorium chains, as well as from decays of common isotopes e.g. ^{40}K, ^{60}Co and ^{137}Cs present in the surrounding materials. The uranium (^{238}U) and thorium (^{232}Th) chains have a series of alpha and beta decays accompanied by the emission of several γ-rays with energies from tens of keV up to 2.6 MeV (highest γ-energy from the thorium chain). The interactions of γ-rays with matter include the photoelectric effect, Compton scattering and e^- e^+ pair production [148]. While the photoelectric effect has the highest cross-section at energies up to few hundred keV, the cross-section for pair production dominates above several MeV. For the energies in between, Compton scattering is the most probable process. All these reactions result in the emission of an electron (or electron and positron for pair production) which can deposit its energy in the target medium. Such energy depositions can be at energies of a few keV affecting the sensitivity of the experiments because this is the energy region of interest for dark matter searches.

Gamma radiation close to the sensitive volume of the detector can be reduced by selecting materials with low radioactive traces. Gamma-spectrometry using high-purity germanium detectors is a common and powerful technique to screen and select radio-pure materials. Other techniques such as mass spectrometry or neutron activation analysis are also used for this purpose [149]. The unavoidable gamma activity from natural radioactivity outside the experimental setup can be shielded by surrounding the detector by a material with a high atomic number and a high density, i.e. good stopping power, and low internal contamination. Lead is a common material used for this purpose. Large water tanks are also employed as they provide a homogeneous shielding as well as the background requirements. To reduce the γ-ray activity from radon in the air, the inner part of the detector shield is either flushed with clean nitrogen or the radon is reduced using a radon trap facility [150].

Analysis tools can be used to further reduce the rate of background interactions. Given the low probability of dark matter particles to interact, the removal of multiple simultaneous hits in the target volume can be, for instance, used for background-event suppression. This

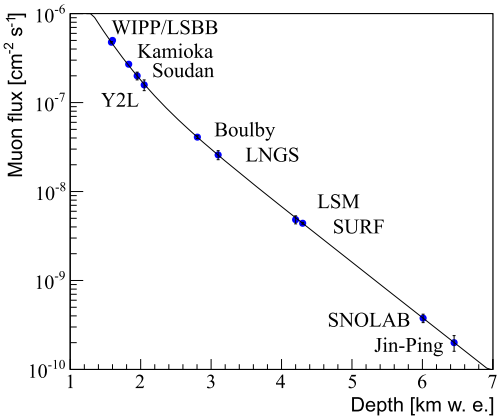

Figure 3. Muon flux as function of depth in kilometres water equivalent (km w. e.) for various underground laboratories hosting dark matter experiments. The effective depth is calculated using the parametrisation curve (thin line) from [151].

includes tagging time-coincident hits in different crystals or identifying multiple scatters in homogeneous detectors. For detectors with sensitivity to the position of the interaction, an innermost volume can be selected for the analysis (fiducial volume). As the penetration range of radiation has an exponential dependence on the distance, most interactions take place close to the surface and background is effectively suppressed. Finally, detectors able to distinguish electronic recoils from nuclear recoils (see section 5.1) can reduce the background by exploiting the corresponding separation parameter.

4.2. Cosmogenic and radiogenic neutron radiation

Neutrons can interact with nuclei in the detector target via elastic scattering producing nuclear recoils. This is a dangerous background because the type of signal is identical to that of the WIMPs. Note that there is also inelastic scattering where the nuclear recoil is typically accompanied by a gamma emission which can be used to tag these events. Cosmogenic neutrons are produced due to spallation reactions of muons on nuclei in the experimental setup or surrounding rock. These neutrons can have energies up to several GeV [151] and are moderated by the detector surrounding materials resulting in MeV energies which can produce nuclear recoils in the energy regime relevant for dark matter searches. In addition, neutrons are emitted in (α, n)- and spontaneous fission reactions from natural radioactivity (called radiogenic neutrons). These neutrons have lower energies of around a few MeV.

Dark matter experiments are typically placed at underground laboratories in order to minimize the number of produced muon-induced neutrons. The deeper the location of the experiment, the lower the muon flux. Figure 3 shows the muon flux as a function of depth for different laboratories hosting dark matter experiments.

The effective depth is calculated using the parametrisation from [151] which is represented by the black line in the figure. The muon flux for each underground location is taken from the corresponding reference of the list below.

- Waste Isolation Pilot Plant (WIPP) [152] in USA.
- Laboratoire Souterrain à Bras Bruit (LSBB) [153] in France.
- Kamioka observatory [151] in Japan.
- Soudan Underground Laboratory [151] in USA.

First results from the DEAP-3600 dark matter search with argon at SNOLAB

P.-A. Amaudruz,[1] M. Baldwin,[2] M. Batygov,[3] B. Beltran,[4] C. E. Bina,[4] D. Bishop,[1] J. Bonatt,[5] G. Boorman,[6] M. G. Boulay,[7,5] B. Broerman,[5] T. Bromwich,[8] J. F. Bueno,[4] A. Butcher,[6] B. Cai,[5] S. Chan,[1] M. Chen,[5] R. Chouinard,[4] B. T. Cleveland,[9,3] D. Cranshaw,[5] K. Dering,[5] J. DiGioseffo,[5] S. Dittmeier,[1] F. A. Duncan,[9,3,†] M. Dunford,[7] A. Erlandson,[7,10] N. Fatemighomi,[6] S. Florian,[5] A. Flower,[7,5] R. J. Ford,[9,3] R. Gagnon,[5] P. Giampa,[5] V. V. Golovko,[10,5] P. Gorel,[4,9,3] R. Gornea,[7] E. Grace,[6] K. Graham,[7] D. R. Grant,[4] E. Gulyev,[1] R. Hakobyan,[4] A. Hall,[6] A. L. Hallin,[4] M. Hamstra,[7,5] P. J. Harvey,[5] C. Hearns,[5] C. J. Jillings,[9,3] O. Kamaev,[10] A. Kemp,[6] M. Kuźniak,[7,5,*] S. Langrock,[3] F. La Zia,[6] B. Lehnert,[7] J. J. Lidgard,[5] C. Lim,[1] T. Lindner,[1] Y. Linn,[1] S. Liu,[4] P. Majewski,[2] R. Mathew,[5] A. B. McDonald,[5] T. McElroy,[4] T. McGinn,[7,5] J. B. McLaughlin,[5] S. Mead,[1] R. Mehdiyev,[7] C. Mielnichuk,[4] J. Monroe,[6] A. Muir,[1] P. Nadeau,[9,5] C. Nantais,[5] C. Ng,[4] A. J. Noble,[5] E. O'Dwyer,[5] C. Ohlmann,[1] K. Olchanski,[1] K. S. Olsen,[4] C. Ouellet,[7] P. Pasuthip,[5] S. J. M. Peeters,[8] T. R. Pollmann,[11,3,5] E. T. Rand,[10] W. Rau,[5] C. Rethmeier,[7] F. Retière,[1] N. Seeburn,[6] B. Shaw,[1] K. Singhrao,[1,4] P. Skensved,[5] B. Smith,[1] N. J. T. Smith,[9,3] T. Sonley,[9,5] J. Soukup,[4] R. Stainforth,[7] C. Stone,[5] V. Strickland,[1,7] B. Sur,[10] J. Tang,[4] J. Taylor,[6] L. Veloce,[5] E. Vázquez-Jáuregui,[12,9,3] J. Walding,[6] M. Ward,[5] S. Westerdale,[7] E. Woolsey,[4] and J. Zielinski[1]

(DEAP-3600 Collaboration)

[1] *TRIUMF, Vancouver, British Columbia, V6T 2A3, Canada*
[2] *Rutherford Appleton Laboratory, Harwell Oxford, Didcot OX11 0QX, United Kingdom*
[3] *Department of Physics and Astronomy, Laurentian University, Sudbury, Ontario, P3E 2C6, Canada*
[4] *Department of Physics, University of Alberta, Edmonton, Alberta, T6G 2R3, Canada*
[5] *Department of Physics, Engineering Physics, and Astronomy, Queen's University, Kingston, Ontario, K7L 3N6, Canada*
[6] *Royal Holloway University London, Egham Hill, Egham, Surrey TW20 0EX, United Kingdom*
[7] *Department of Physics, Carleton University, Ottawa, Ontario, K1S 5B6, Canada*
[8] *University of Sussex, Sussex House, Brighton, East Sussex BN1 9RH, United Kingdom*
[9] *SNOLAB, Lively, Ontario, P3Y 1M3, Canada*
[10] *Canadian Nuclear Laboratories Ltd, Chalk River, Ontario, K0J 1J0, Canada*
[11] *Department of Physics, Technische Universität München, 80333 Munich, Germany*
[12] *Instituto de Física, Universidad Nacional Autónoma de México, A. P. 20-364, México D. F. 01000, Mexico*

(Dated: August 1, 2017)

This paper reports the first results of a direct dark matter search with the DEAP-3600 single-phase liquid argon (LAr) detector. The experiment was performed 2 km underground at SNOLAB (Sudbury, Canada) utilizing a large target mass, with the LAr target contained in a spherical acrylic vessel of 3600 kg capacity. The LAr is viewed by an array of PMTs, which would register scintillation light produced by rare nuclear recoil signals induced by dark matter particle scattering. An analysis of 4.44 live days (fiducial exposure of 9.87 tonne·days) of data taken with the nearly full detector during the initial filling phase demonstrates the detector performance and the best electronic recoil rejection using pulse-shape discrimination in argon, with leakage $<1.2\times10^{-7}$ (90% C.L.) between 16 and 33 $\mathrm{keV_{ee}}$. No candidate signal events are observed, which results in the leading limit on WIMP-nucleon spin-independent cross section on argon, $<1.2\times10^{-44}$ cm^2 for a 100 GeV/c^2 WIMP mass (90% C.L.).

PACS numbers: 95.35+d, 29.40.Mc, 26.65.+t, 34.50.Gb, 07.20.Mc, 12.60.Jv

It is well established from astronomical observations that *dark matter* (DM) constitutes most of the matter in the Universe [1], accounting for 26.8% of the energy density, compared to 4.9% for ordinary matter. Weakly Interacting Massive Particles (WIMPs) are one of the leading dark matter candidates, predicted by a number of theoretical extensions of the Standard Model. Direct detection of WIMPs from the galactic halo is possible via elastic scattering interactions, which produce nuclear recoils of a few tens of keV. Such detection requires large target mass in ultralow background detectors located deep underground to suppress background associated with cosmic rays.

This paper reports on the analysis of commissioning data from DEAP-3600, the first liquid argon (LAr) based dark matter detector exceeding a 1 tonne target mass. DEAP-3600 uses single-phase technology, which registers only the primary scintillation light from the target medium. We determine the best limit on WIMP-nucleon cross section measured with argon, in the high WIMP mass regime second only to xenon based searches, and demonstrate the best low-threshold electronic recoil re-

jection using pulse-shape discrimination (PSD) in argon. The substantial difference in LAr scintillation timing between nuclear recoils (NR) and electronic recoils (ER) allows sufficient rejection of the dominant β/γ backgrounds [2, 3] using only the primary scintillation light. The DEAP-3600 single phase LAr detector design offers excellent scalability to ktonne-scale target masses [4, 5].

The detector is comprised of an atmospheric LAr target contained in a transparent acrylic vessel (AV) cryostat capable of storing 3600 kg of argon. The AV is viewed by 255 Hamamatsu R5912-HQE photomultiplier tubes (PMTs) operated near room temperature to detect scintillation light generated in the target medium. The PMTs are coupled to the AV by 50 cm-long acrylic light guides (LGs) that also provide neutron shielding and reduce the heat load on the AV. The inner AV surface was coated in-situ with a thin layer of wavelength shifter, 1,1,4,4-tetraphenyl-1,3-butadiene (TPB) to convert 128 nm Ar scintillation light into visible blue light, which is efficiently transmitted through acrylic. The AV neck is wrapped with optical fibers read out by 4 PMTs from both ends, to veto light emission in the AV neck region. The detector is housed in a stainless steel spherical shell, which is immersed in an 8 m diameter ultrapure water tank instrumented with 48 PMTs. This tank serves as a radiation shield and Cherenkov veto for cosmogenic muons. All detector materials were selected to achieve the background target of <0.6 events in a 3 tonne-year exposure [5]. To avoid ^{222}Rn/^{210}Pb contamination of the bulk acrylic and TPB, the inner 0.5 mm surface layer of the inner AV was removed in-situ after construction. The Rn exposure was then strictly limited, with the AV and the access glovebox purged with Rn-scrubbed N_2, evacuated and baked before filling. Argon was delivered as cryogenic liquid, stored underground, purified as gas with SAES Megatorr PS5 to sub-ppb impurity levels (for O_2, H_2O, CO, CO_2, H_2, N_2 and hydrocarbons), scrubbed of Rn [6] and liquified in the AV.

PMT signals are decoupled from the high voltage by a set of custom analog signal-conditioning boards and split into three outputs: high- and low-gain, and a twelve channel analog sum used to generate trigger decisions. Outputs are digitized with CAEN V1720 digitizers and handled by the MIDAS DAQ system, described in [7].

The PMT charge response functions are calibrated daily with a system of optical fibres injecting 435 nm light from a pulsed LED source onto 20 PMTs uniformly spaced around the detector (and 2 additional fibres in the detector neck), allowing study of a range of occupancies in all PMTs with a combination of reflected and direct illumination. A detailed model of the charge response function for each PMT gives the mean single photoelectron (SPE) charges with uncertainty less than 3% [5, 8]. A full PMT signal simulation is implemented in a detailed Monte Carlo model of the detector and electronics, using the GEANT4-based RAT [9]. For accurate simulation of PSD, the PMT simulation uses in-situ measured time vs. charge distributions from calibration data for noise sources, including late, double, and after-pulsing (AP) for each PMT [5, 8, 10].

The charge of each identified pulse is divided by the PMT-specific mean SPE charge to extract the number of photoelectrons (PEs). F_{prompt} is then defined for each event as the ratio of prompt to total charge,

$$F_{prompt} \equiv \frac{\sum_{\{i|t_i\in(-28\ ns,150\ ns)\}} Q_i}{\sum_{\{i|t_i\in(-28\ ns,10\ \mu s)\}} Q_i}, \quad (1)$$

where Q is the pulse charge in PE and t is the pulse time with respect to the event time. The relative timing of each PMT channel is calibrated with a fast laser source; the resulting overall time resolution is 1.0 ns. F_{prompt} is a powerful PSD variable because it is sensitive to the ratio of excited singlet to triplet states in LAr, with lifetimes of 6 and 1300 ns [11], respectively.

The detector trigger was designed to accept all low energy events above threshold, all high-F_{prompt} NR events and to cope with approx. 1 Bq/kg ^{39}Ar activity of LAr [12], by prescaling the resulting low-F_{prompt} ER events. The signal from the inner PMT analog sum is continuously integrated in windows 177 ns and 3100 ns wide, from which the prompt energy ($E_{trigger}$) and ratio of prompt and wide energies ($F_{trigger}$) are calculated. Triggers with NR-like $E_{trigger}$ >40 PE are digitized for all events, while only 1% of ^{39}Ar-decay-like events are digitized; summary information is recorded for all events. While for NR-like events in this analysis the trigger is highly efficient, $(100^{+0.0}_{-0.1})$%, as determined by running in a very low threshold mode, for ER-like events below 120 PE the efficiency decreases because of their lower prompt charge. This result was validated with a dedicated random trigger run, processed offline with a simulated physics trigger algorithm.

Stability of the LAr triplet lifetime, τ_3, was verified with a fit accounting for PMT AP, dark noise, and TPB fluorescence [13]. From this fit τ_3=1399±20 (PMT syst.)±8 (fit syst.)±6 (TPB syst.)±7(AP syst.) ns, where systematic uncertainties are evaluated by performing the fit separately on individual PMTs, varying the fit range, and varying the TPB fluorescence decay time and times of the AP distributions within uncertainties. This result is consistent with the literature value of 1300±60 ns [11] and is stable throughout the analyzed dataset. Stability over a longer period is shown in Fig. S1.

The dominant source of scintillation events is ^{39}Ar β decay, resulting in low-F_{prompt} ER events. In order to define an F_{prompt} cut constraining the leakage of ^{39}Ar events into the NR band, the F_{prompt} distribution of ER and its energy dependence were fitted with an 11-parameter empirical model of F_{prompt} vs. PE, based on a smeared Gamma distribution,

$$\mathrm{PSD}(n,f) = \Gamma(f;\overline{f}(n),b(n)) \otimes \mathrm{Gauss}(f;\sigma(n)), \quad (2)$$

where $b(n) = a_0 + \frac{a_1}{n} + \frac{a_2}{n^2}$, $\sigma(n) = a_3 + \frac{a_4}{n} + \frac{a_5}{n^2}$ and $\overline{f}(n)$ is parametrized as $a_6 + \frac{a_7}{n-a_8} + \frac{a_9}{(n-a_{10})^2}$. The 2-dimensional fit of the model to the data from 80 to 260 PE has a χ^2_{ndf} of 5581/(5236-11). As an example, a 1-dimensional slice from the model and the data at 80 PE is shown in Fig. 1(a). The PSD leakage measured in the 120 to 240 PE window with a 90% NR acceptance is shown in Fig. 1(b). The extrapolated leakage is approximately 10 times lower than projected in the DEAP-3600 design [3]. As further reduction in the PSD leakage is expected from an analysis relying on SPE counting [14], the original goal of a 120 PE analysis threshold in 3 years livetime from PSD will likely be surpassed.

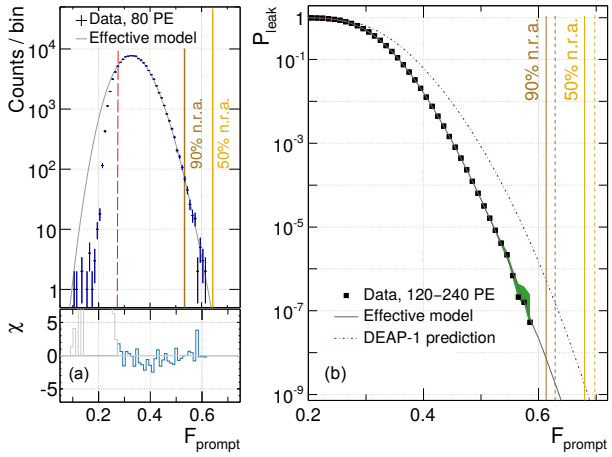

FIG. 1: (a) Projection of the F_{prompt} distribution at 80 PE (full 2-dimensional distribution is shown in Fig. 5) is shown together with the effective model. Fit is performed above the red dashed line, indicating the F_{prompt} value below which the trigger efficiency is <100%. The brown and orange lines correspond to 90% and 50% NR acceptance (n.r.a.). Each PE bin in the fit range contributes approximately equally to the overall χ^2 value. (b) Data and model for the 120-240 PE range with 1.87972×10^7 events, represented as leakage probability above a given F_{prompt} value. A conservative projection from DEAP-1 [3] is also shown with its own NR acceptance lines (all three dashed).

The energy calibration uses internal detector backgrounds and external radioactive sources. The internal calibration uses β's from ^{39}Ar decay, with an endpoint of 565 keV. These are uniformly distributed in the detector, as WIMP-induced NR's would be. The external calibration uses a ^{22}Na source, which produces 1.27 MeV γ's and a 30-50 keV photo-absorption feature, both near the AV surface, similar to surface backgrounds. The simulated spectra of ^{39}Ar and ^{22}Na are fit to the data to find the energy response function relating $T_{\rm eff}$ [$\rm keV_{ee}$] (electron-equivalent energy) to detected PE,

$$T_{\rm eff}(\rm PE) = 1.15 + 0.121\ \rm PE + 1.32\times10^{-6}\ \rm PE^2. \quad (3)$$

The internal and external sources are fit separately, because of their different spatial distributions. The error bars on the fit parameters are scaled by $\sqrt{\chi^2_{ndf}}$ to account for the systematic uncertainty, and the best fit values are combined in a weighted average to produce the final response function, which is shown in Fig. 2 together with the ^{39}Ar data, which spans from below to above the energy window for this analysis (see Fig. S2 for the ^{22}Na fit). The energy response function fits for ^{39}Ar and ^{22}Na agree within errors, however an additional systematic uncertainty, 0.5 $\rm keV_{ee}$ is assessed to account for the non-zero offset term. As a cross-check, the response function is extrapolated to compare with high energy γ lines, particularly 1461 keV from ^{40}K and 2614 keV from ^{208}Tl in the detector materials, showing good agreement until ^{40}K and then diverging in the regime where PMT saturation and non-linearities in the DAQ become more significant. The light yield (LY) at 80 PE is $7.36^{+0.61}_{-0.52}$(fit syst.)±0.22(SPE syst.) $\rm PE/keV_{ee}$, where systematic uncertainties from the fitting procedure and the SPE charge calibration are included.

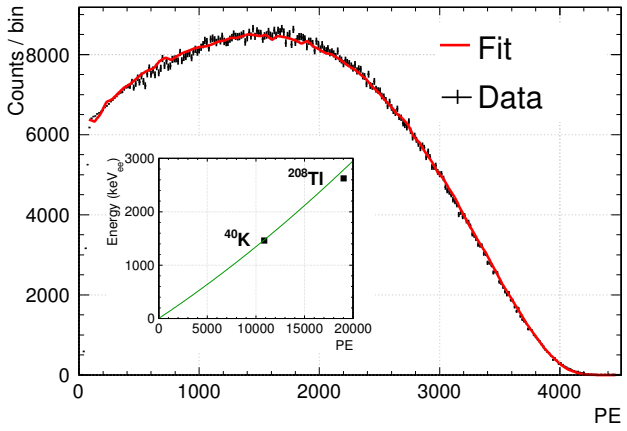

FIG. 2: Measured ^{39}Ar β spectrum overlayed with the fit function (red) based on simulation, see text. The inset shows the global energy reponse function from weighted average of ^{39}Ar and ^{22}Na fits, $T_{\rm eff}(\rm PE) = c_0 + c_1\rm PE + c_2\rm PE^2$, with c_0=1.15±0.50 $\rm keV_{ee}$, c_1=0.121±0.004 $\rm keV_{ee}PE^{-1}$ and c_2=(1.32±0.08)×10^{-6} $\rm keV_{ee}PE^{-2}$. As a cross check, on the inset γ lines from ^{40}K and ^{208}Tl are compared with the extrapolated function; ^{208}Tl diverges from the function because of PMT/DAQ saturation effects.

A Gaussian energy resolution function is used to smear the spectra in the fit, with variance $\sigma^2 = p_1 \cdot \rm PE$. Extrapolated resolution at 80 PE from best fit values for ^{39}Ar and ^{22}Na is 13±1% and 16±1%, respectively. The difference is attributed to a larger spread in light collection efficiency for events near the AV surface as measured with the ^{22}Na source. A lower bound on the energy resolution at 80 PE is 12% (p_1 = 1.185), determined from Poisson counting statistics widened by the measured in-situ SPE charge resolution. Since at low WIMP masses

the broader the resolution the stronger the limit, because of the steeply falling WIMP-induced NR spectrum, using this lower bound is conservative.

The nuclear recoil acceptance of the F_{prompt} cut is determined from a simulation of ^{40}Ar recoils distributed uniformly in LAr. The simulation assumes the quenching factor and triplet/singlet ratio energy dependence as measured by SCENE [15] at zero electric field and applies the full response of the detection and analysis chain. PMT AP dominates the effect of the detector response on the mean F_{prompt} with the average AP probability of (7.6±1.9)% [5]. Comparison of external neutron AmBe source data with a simplified detector simulation in Fig. 3(b) shows qualitative agreement and serves as a validation of the model. The simulation includes neutrons and 4.4 MeV γ's from the AmBe source and considers scattering- or capture induced γ's only for neutrons that entered the LAr. AmBe data is not used directly to model the WIMP-induced NR acceptance as a significant fraction (59% in the 120-240 PE window) of AmBe events contain multiple elastic neutron scatters.

The region-of-interest (ROI) in this analysis, as shown in Fig. 3(a), was defined by allowing for an expectation of 0.2 leakage events from the ^{39}Ar band, determined with the PSD model, while maintaining the NR acceptance of >5% at the lowest energies. The smaller number of ^{39}Ar events in the short exposure and the low F_{prompt} leakage allowed us to set the energy threshold at 80 PE (11 keV_{ee}), lower than the nominal 120 PE threshold originally projected [3]. Above 150 PE the lower limit on F_{prompt} is chosen to remove 5% of NR events in each bin. The ROI also has a maximum F_{prompt} chosen to remove 1% of NR events in each 1 PE bin. The maximum energy was set to 240 PE to reduce possible backgrounds from α activity of the AV surface [16].

The first LAr fill of the detector took approx. 100 days between May and mid-August 2016. For the majority of this time, Ar gas was introduced into the detector from the purification system for cooling. In the final phase of the fill, shortly after the dataset discussed in this work was taken, a leak in the detector neck contaminated LAr with clean Rn-scrubbed N_2. The detector was subsequently emptied and refilled and has been taking data since Nov. 1, 2016, with a slightly lower liquid level.

In this work, we focus on the period Aug. 5 to Aug. 15 (9.09 days), when no Ar had been introduced into the detector. Because of the much higher scintillation rate, photon yield and refractive index in liquid than in gas, there is a very sharp drop in rate between PMTs facing the liquid and PMTs facing the vapour space, which allows determination of the fill level, 590±50 mm above the AV centre, and the full LAr mass, 3322±110 kg.

Calibration data used were collected after the 2nd fill: 23 h of ^{22}Na (Nov. 3-4) and 65 h of AmBe data (Dec. 2-4).

Data were analyzed from runs where (1) the difference between the maximum and minimum AV pressures in a run corresponded to <1 cm change in the liquid level and (2) no more than one PMT read <50% of its average charge, determined from approx. 5 min samples. During this dataset one PMT was turned off (and has since returned to operation). In all cases, pressure excursions were correlated with periods of the cryocoolers operating at reduced power. 34% of the data are removed by failing both criteria and additional 11% by failing criterion 2 alone. The total run time after run selection corresponds to 4.72 d, out of which 0.28 days (5.9%) is deadtime from 17.5 μs following each trigger.

Acceptance for NR events, shown in Fig. 4, is determined using a combination of ^{39}Ar events, which are uniformly distributed in the LAr volume, and simulation of F_{prompt} for NR events. The sample of ^{39}Ar single-recoils is obtained first by applying low level cuts to remove events (1) from DAQ calibration, (2) highly asymmetric (with more than 40% of charge in a single PMT) e.g. Cherenkov events in LGs and PMTs or (3) from pile-up. The approach of measuring acceptance for NR events using ER events is used since none of the acceptance cut variables depend on the pulse time information, only F_{prompt} does, which is handled separately. The F_{prompt} simulation for NR's is validated by comparison with the AmBe calibration data.

Quality cuts are applied to ^{39}Ar events within the energy window in order to determine the ER acceptance, as shown in Table I. The fiducial acceptance is determined with respect to the events remaining after the quality cuts in order to factor out light coming from outside the LAr volume. The event time cut requires that the scintillation peak is positioned early in the waveform, which ensures reliable evaluation of F_{prompt}. Cuts on the fraction of charge in the brightest PMT and on the neck veto remove high charge afterpulses triggering the detector as well as events caused by light emission (e.g. Cherenkov) in the AV neck acrylic. We have identified a class of background events originating in the neck region and are characterizing it for future larger-exposure searches.

Fiducialization in this analysis employs low-level PE ratio variables. These are the fraction of scintillation-induced PE [14] with AP correction [10] in the PMT in a given event detecting the most light, and the fraction of charge in the top 2 rows of PMTs in the detector. These are strongly correlated with the radial and vertical event positions, respectively. The fiducial mass, 2223±74 kg, is determined from the full LAr mass and acceptance of the fiducial cuts. The expected activity of ^{39}Ar contained in this mass is 2245±198 Bq [12], consistent with the fiducial rate observed in DEAP-3600, 2239±8 Hz.

Position reconstruction algorithms have been developed and tested on the detector data. However, in the analysis presented here, they are used only as a cross-check. A maximum likelihood fitter relies on the full Monte Carlo of the detector including its optical properties, and minimizes the difference between the observed

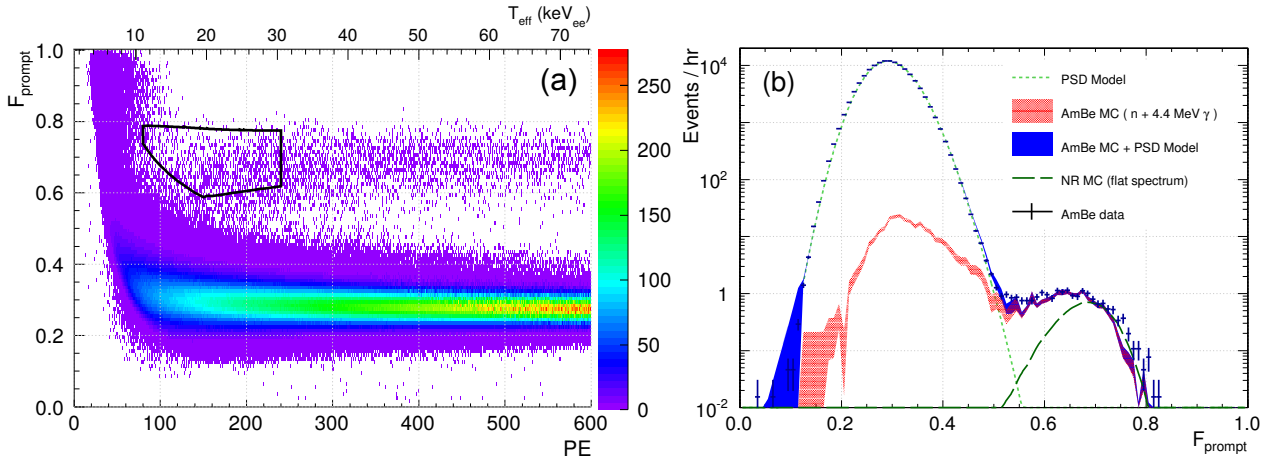

FIG. 3: (a) AmBe source data after cuts, with the region-of-interest for WIMP search shown with a black box. (b) The F_{prompt} distribution for 140<PE<240 in AmBe calibration data (black), compared to summed simulated contributions for AmBe neutrons, and 4.4 MeV γ's and the ^{39}Ar F_{prompt} model normalized to the peak of the distribution. Also plotted is the simulation of single scatter nuclear recoils with flat energy spectrum (see legend). Error bars shown on the simulated distributions are statistical, not systematic.

	Cut	Livetime	Acceptance %		$\#^{ROI}_{evt.}$
run	Physics runs	8.55 d			
	Stable cryocooler	5.63 d			
	Stable PMT	4.72 d			
	Deadtime corrected	4.44 d			119181
low level	DAQ calibration				115782
	Pile-up				100700
	Event asymmetry				787
quality	Max charge fraction per PMT		99.58±0.01		654
	Event time		99.85±0.01		652
	Neck veto		$97.49^{+0.03}_{-0.05}$		23
fiducial	Max scintillation PE fraction per PMT			$75.08^{+0.09}_{-0.06}$	7
	Charge fraction in the top 2 PMT rings			$90.92^{+0.11}_{-0.10}$	0
	Total	4.44 d	96.94±0.03	$66.91^{+0.20}_{-0.15}$	0

TABLE I: Run selection criteria and cuts with their effects on livetime, integrated acceptance, the fiducial fraction, and the number of events left in the ROI. The acceptance is calculated individually for each run and then weighted by livetime to provide an overall acceptance with the uncertainties taken as maximum and minimum variations about this weighted mean from each run. See text for details about the fiducial fraction determination. The total number of triggers before any cuts was 1.38×10^9, out of which 6.47×10^7 in 80-240 PE window.

pattern of PMT charges and the one expected based on a PDF constructed from simulation, under the assumption that the illumination of the detector is symmetric around the axis of the event position vector. Residual position bias is corrected for using the uniformly distributed population of ^{39}Ar β's. To study reconstruction of events from the inner AV surface, as expected for α backgrounds, we apply the ^{39}Ar-derived calibration to ^{22}Na events, which are strongly peaked near the surface. Fig. S3 shows that qualitative agreement results from this procedure. We plan to use reconstructed positions to further reduce backgrounds in longer exposure runs.

The main background sources are α activity, neutrons, leakage from ^{39}Ar and other ER interactions.

As shown in Table II, ^{222}Rn, ^{218}Po and ^{214}Po α decays can be identified in the LAr bulk in well-defined high energy peaks with an activity of 1.8×10^{-1} μBq/kg based on time delayed coincidence with α-α (^{222}Rn-^{218}Po and ^{220}Rn-^{216}Po) or β-α (^{214}Bi-^{214}Po) tags. The activity of ^{214}Po in the bulk is consistent with the earlier part of the chain, which indicates that it is mostly mixed within the LAr volume, see Table II and Fig. S4. Out-of-equilibrium ^{210}Po α decays can be identified with degraded energies characteristic of α's coming from below the 3 μm thick TPB layer on the surface of the acrylic. Activity of ^{210}Po is determined with a fit of simulated spectra to the data (see Fig. S5), assuming contamination either on the acrylic surface or distributed uniformly in an 80 μm deep acrylic surface layer. The result for bulk contamination assumes no additional backgrounds in the fit range and is considered an upper limit.

The dominant source of neutron events is expected to be from (α, n) reactions and spontaneous fission in the PMTs. The PMT borosilicate glass contribution can be constrained with in-situ measurements of the 2614 keV and 1764 keV γ-rays from the ^{232}Th and ^{238}U decay chains, respectively. The ^{238}U and ^{232}Th decay chain activities seen in-situ agree within a factor of two with a simulation based on the screening results. Events from neutron backgrounds in LAr can be measured in-situ by

Component	Activity	
^{222}Rn LAr	$(1.8\pm0.2)\times10^{-1}$	µBq/kg
^{214}Po LAr	$(2.0\pm0.2)\times10^{-1}$	µBq/kg
^{220}Rn LAr	$(2.6\pm1.5)\times10^{-3}$	µBq/kg
^{210}Po AV surface	0.22 ± 0.04	mBq/m^2
^{210}Po AV bulk	<2.2	mBq

TABLE II: Summary of α activities, see text. These can be compared with results reported by other experiments, approx.: 66 µHz/kg of ^{222}Rn and 10 µHz/kg of ^{220}Rn in LUX [17], 6.57 µBq/kg of ^{222}Rn and 0.41 µBq/kg of ^{220}Rn in PandaX-II [18], and 10 µBq/kg of ^{222}Rn in XENON1T [19].

searching for NR's followed by capture γ's. The efficiency of this technique was calibrated using neutrons from an AmBe source deployed near the PMTs. No neutron candidates were seen in 4.44 d (80-10000 PE window, no fiducial cuts), which is consistent with the expectation based on assays.

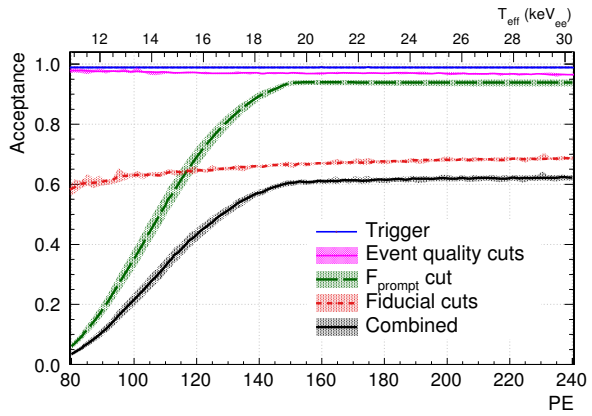

FIG. 4: The acceptance with systematic error bands in 80-240 PE window for the trigger, event quality cuts, F_{prompt} cut, fiducial cuts and all cuts combined. For uncertainties on the acceptance of quality and fiducial cuts see also Table I. Uncertainties on trigger acceptance measurement and F_{prompt} cut acceptance are discussed in the text.

The systematic uncertainties considered in the WIMP cross-section limit calculation include uncertainty on the NR energy response, exposure (from livetime and total LAr mass), and quality and fiducial cut acceptance (see Fig. 4). The uncertainty on the NR acceptance of the F_{prompt} cut is determined by varying the simulation inputs: triplet/singlet ratio (within errors propagated from the SCENE [15] measurement of f_{90}), the triplet lifetime uncertainty (the difference between literature value [11] and this work), and the AP probability. The dominant uncertainty in the final exclusion curve comes from the uncertainty on the NR energy response. This effect is dominated by uncertainties in Eq. (3); however, there is also some uncertainty on the NR quenching factor, i.e. the reduction in NR scintillation yield relative to ER. ($[\mathrm{keV_r}] = \mathcal{L}_{\mathrm{eff}} \cdot [\mathrm{keV_{ee}}]$, when referring to energies of NR, $\mathrm{keV_r}$, the unit of the full energy of the recoil, can be used.) We used measurements from SCENE, which reports two different quenching factors: $\mathcal{L}_{\mathrm{eff},^{83m}\mathrm{Kr}}$, which is the ratio of LY measurement at various NR energies to the LY measured by a ^{83m}Kr ER calibration, and $\mathcal{L}$, which is the Lindhard-Birks quenching factor describing the suppression of quanta (scintillation photons or extracted electrons) at different NR energies. The difference between these two values at a given NR energy is due to non-unitary recombination at null field. We adjusted the Lindhard-Birks quenching factors fit to $\mathcal{L}$ to account for the relative recombination rates of NR and ^{83m}Kr ER at null field, according to the NEST model [20], fitting Thomas-Imel and Doke-Birks recombination parameters to SCENE's $\mathcal{L}_{\mathrm{eff},^{83m}\mathrm{Kr}}$ values. Uncertainties on this fit were inflated to account for differences between the SCENE and DEAP-3600 detectors and the different recombination rates of the ^{83m}Kr ER and the ^{22}Na low energy feature that we used for our energy calibration. These factors, along with uncertainty in SCENE's reported value of Birks' constant and the difference between $\mathcal{L}$ and $\mathcal{L}_{\mathrm{eff},^{83m}\mathrm{Kr}}$ were factored into the uncertainty of our quenching factor, to account for uncertainties in the recombination probabilities.

No events are observed in the ROI, see Fig. 5. Figure 6 shows the resulting upper limit on the spin-independent WIMP-nucleon scattering cross-section as a function of WIMP mass, based on the standard DM halo model [21]. A 90% C.L. upper limit is derived after factoring in the Poisson fluctuation in the number of expected signal events, with the Highland-Cousins [22] method employed to account for the systematic uncertainties. For a more conservative limit, the backgrounds from ^{39}Ar leakage were not taken into account.

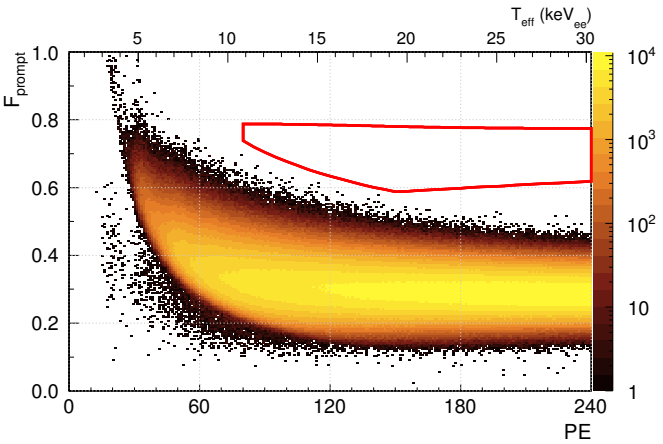

FIG. 5: F_{prompt} vs the number of photoelectrons and energy in $\mathrm{keV_{ee}}$ for events passing cuts, with the WIMP search ROI shown in red.

DEAP-3600 has achieved stable operation at

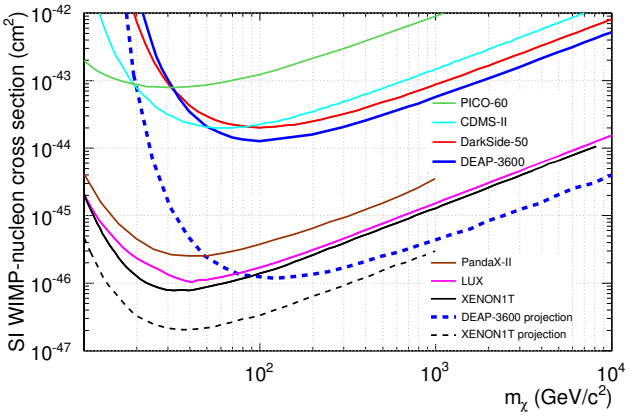

FIG. 6: Spin-independent WIMP-nucleon cross-section 90% C.L. exclusion from 4.44 live days of DEAP-3600 data. Also shown: the current results from XENON1T [23], LUX [24], PandaX-II [25], DarkSide-50 [26], CDMS-II [28], PICO-60 [27], and the full sensitivity for XENON1T and DEAP-3600, assuming no observed events in a fiducial volume of 1000 kg in three years of running with a threshold of 15 keV$_{ee}$.

7.36 PE/keV$_{ee}$ light yield without recirculation, and demonstrated better-than-expected PSD (permitting a 39 keV$_r$ energy threshold), with promising α and neutron background levels. Analysis of the first 4.44 d of data reported here results in the best limit at low energies on discrimination of β-decay backgrounds using PSD in LAr at 90% NR acceptance, with measured leakage probability of $<1.2\times10^{-7}$ (90% C.L.) in the energy window 16-33 keV$_{ee}$ (55-111 keV$_r$). This measurement has lower threshold than DEAP-1 [3] and higher statistics than DarkSide-50 [26]. After NR selection cuts no events are observed, resulting in the best spin-independent WIMP-nucleon cross section limit measured in LAr [26] of $<1.2\times10^{-44}$ cm^2 for a 100 GeV/c^2 WIMP (90% C.L.). Data collection has been ongoing since Nov. 2016 and forms the basis for a more sensitive DM search currently in progress.

This work is supported by the Natural Sciences and Engineering Research Council of Canada, the Canadian Foundation for Innovation (CFI), the Ontario Ministry of Research and Innovation (MRI), and Alberta Advanced Education and Technology (ASRIP), Queen's University, University of Alberta, Carleton University, DGAPA-UNAM (PAPIIT No. IA100316), European Research Council (ERC StG 279980), the UK Science & Technology Facilities Council (STFC) (ST/K002570/1), the Leverhulme Trust (ECF-20130496). Studentship support by the Rutherford Appleton Laboratory Particle Physics Division, STFC and SEPNet PhD is acknowledged. We thank SNOLAB and its staff for support through underground space, logistical and technical services. SNOLAB operations are supported by CFI and the Province of Ontario MRI, with underground access provided by Vale at the Creighton mine site. We thank Compute Canada, Calcul Québec and the Center for Advanced Computing at Queen's University for providing the excellent computing resources required to undertake this work.

† Deceased.
* Electronic address: mkuzniak@physics.carleton.ca

[1] P. A. R. Ade et al. (Planck), A&A **594**, A13 (2016)
[2] M. G. Boulay, A. Hime, Astropart.Phys. **25**, 179 (2006)
[3] P.-A. Amaudruz et al., Astropart. Phys. **85**, 1 (2016)
[4] M. Kuźniak et al., Nucl.Part.Phys.Proc.**273**, 340 (2016)
[5] P.-A. Amaudruz et al., to be submitted to Astroparticle Physics.
[6] E. O'Dwyer, M.Sc. thesis, Queen's University, 2011.
[7] T. Lindner (DEAP), J.Phys.Conf.Ser. **664**, 82026 (2015)
[8] P.-A. Amaudruz et al., arXiv:1705.10183 (2017)
[9] T. Caldwell, talk at AARM Meeting, Fermilab, March 19-22 (2014), https://zzz.physics.umn.edu/lowrad/_media/meeting7/rat_aarm_2014.pdf
[10] A. Butcher et al., arXiv:1703.06204 (2017)
[11] T. Heindl et al., EPL **91**, 62002 (2010)
[12] P. Benetti et al., NIM A **574**, 83 (2007)
[13] E. Segreto, Phys. Rev. C **91**, 035503 (2015)
[14] M. Akashi-Ronquest et al., Astropart.Phys. **65**, 40 (2015)
[15] H. Cao et al., Phys. Rev. D **91**, 092007 (2015)
[16] P.-A. Amaudruz et al., Astropart. Phys. **62**, 178 (2015)
[17] A. Bradley et al., Phys. Procedia **61**, 658 (2015)
[18] A. Tan et al., Phys. Rev. D **93**, 122009 (2016)
[19] P. A. Breur, talk at XeSAT 2017, April 3-7, https://indico.cern.ch/event/573069/sessions/230077/attachments/1440290/2217054/170404_Xesat_Radon_signals_in_XENON1T_presentation_FINAL.pdf
[20] M. Szydagis et al., JINST **6**, P10002 (2011)
[21] C. McCabe, Phys. Rev. D **82**, 023530 (2010)
[22] R. D. Cousins, V. L. Highland, NIM A **320**, 331 (1992)
[23] E. Aprile et al., arXiv:1705.06655 (2017)
[24] D. S. Akerib, Phys. Rev. Lett. **118**, 021303 (2017)
[25] A. Tan et al., Phys. Rev. Lett. **117**, 121303 (2016)
[26] P. Agnes et al., Phys. Rev. D **93**, 081101 (2016)
[27] C. Amole, Phys. Rev. Lett. **118**, 251301 (2017)
[28] R. Agnese, Phys. Rev. D **92**, 072003 (2015).

First Dark Matter Search Results from the XENON1T Experiment

E. Aprile,[1] J. Aalbers,[2,*] F. Agostini,[3,4] M. Alfonsi,[5] F. D. Amaro,[6] M. Anthony,[1] F. Arneodo,[7] P. Barrow,[8] L. Baudis,[8] B. Bauermeister,[9] M. L. Benabderrahmane,[7] T. Berger,[10] P. A. Breur,[2] A. Brown,[2] A. Brown,[8] E. Brown,[10] S. Bruenner,[11] G. Bruno,[3] R. Budnik,[12] L. Bütikofer,[13,†] J. Calvén,[9] J. M. R. Cardoso,[6] M. Cervantes,[14] D. Cichon,[11] D. Coderre,[13] A. P. Colijn,[2] J. Conrad,[9,‡] J. P. Cussonneau,[15] M. P. Decowski,[2] P. de Perio,[1] P. Di Gangi,[4] A. Di Giovanni,[7] S. Diglio,[15] G. Eurin,[11] J. Fei,[16] A. D. Ferella,[9] A. Fieguth,[17] W. Fulgione,[3,18] A. Gallo Rosso,[3] M. Galloway,[8] F. Gao,[1] M. Garbini,[4] R. Gardner,[19] C. Geis,[5] L. W. Goetzke,[1] L. Grandi,[19] Z. Greene,[1] C. Grignon,[5] C. Hasterok,[11] E. Hogenbirk,[2] J. Howlett,[1] R. Itay,[12] B. Kaminsky,[13,†] S. Kazama,[8] G. Kessler,[8] A. Kish,[8] H. Landsman,[12] R. F. Lang,[14] D. Lellouch,[12] L. Levinson,[12] Q. Lin,[1] S. Lindemann,[11,13] M. Lindner,[11] F. Lombardi,[16] J. A. M. Lopes,[6,§] A. Manfredini,[12] I. Mariş,[7] T. Marrodán Undagoitia,[11] J. Masbou,[15] F. V. Massoli,[4] D. Masson,[14] D. Mayani,[8] M. Messina,[1] K. Micheneau,[15] A. Molinario,[3] K. Morå,[9] M. Murra,[17] J. Naganoma,[20] K. Ni,[16] U. Oberlack,[5] P. Pakarha,[8] B. Pelssers,[9] R. Persiani,[15] F. Piastra,[8] J. Pienaar,[14] V. Pizzella,[11] M.-C. Piro,[10] G. Plante,[1,¶] N. Priel,[12] L. Rauch,[11] S. Reichard,[8,14] C. Reuter,[14] B. Riedel,[19] A. Rizzo,[1] S. Rosendahl,[17] N. Rupp,[11] R. Saldanha,[19] J. M. F. dos Santos,[6] G. Sartorelli,[4] M. Scheibelhut,[5] S. Schindler,[5] J. Schreiner,[11] M. Schumann,[13] L. Scotto Lavina,[21] M. Selvi,[4] P. Shagin,[20] E. Shockley,[19] M. Silva,[6] H. Simgen,[11] M. v. Sivers,[13,†] A. Stein,[22] S. Thapa,[19] D. Thers,[15] A. Tiseni,[2] G. Trinchero,[18] C. Tunnell,[19,**] M. Vargas,[17] N. Upole,[19] H. Wang,[22] Z. Wang,[3] Y. Wei,[8] C. Weinheimer,[17] J. Wulf,[8] J. Ye,[16] Y. Zhang,[1] and T. Zhu[1]

(XENON Collaboration),[††]

[1]*Physics Department, Columbia University, New York, NY 10027, USA*
[2]*Nikhef and the University of Amsterdam, Science Park, 1098XG Amsterdam, Netherlands*
[3]*INFN-Laboratori Nazionali del Gran Sasso and Gran Sasso Science Institute, 67100 L'Aquila, Italy*
[4]*Department of Physics and Astrophysics, University of Bologna and INFN-Bologna, 40126 Bologna, Italy*
[5]*Institut für Physik & Exzellenzcluster PRISMA, Johannes Gutenberg-Universität Mainz, 55099 Mainz, Germany*
[6]*LIBPhys, Department of Physics, University of Coimbra, 3004-516 Coimbra, Portugal*
[7]*New York University Abu Dhabi, Abu Dhabi, United Arab Emirates*
[8]*Physik-Institut, University of Zurich, 8057 Zurich, Switzerland*
[9]*Oskar Klein Centre, Department of Physics, Stockholm University, AlbaNova, Stockholm SE-10691, Sweden*
[10]*Department of Physics, Applied Physics and Astronomy, Rensselaer Polytechnic Institute, Troy, NY 12180, USA*
[11]*Max-Planck-Institut für Kernphysik, 69117 Heidelberg, Germany*
[12]*Department of Particle Physics and Astrophysics, Weizmann Institute of Science, Rehovot 7610001, Israel*
[13]*Physikalisches Institut, Universität Freiburg, 79104 Freiburg, Germany*
[14]*Department of Physics and Astronomy, Purdue University, West Lafayette, IN 47907, USA*
[15]*SUBATECH, IMT Atlantique, CNRS/IN2P3, Université de Nantes, Nantes 44307, France*
[16]*Department of Physics, University of California, San Diego, CA 92093, USA*
[17]*Institut für Kernphysik, Westfälische Wilhelms-Universität Münster, 48149 Münster, Germany*
[18]*INFN-Torino and Osservatorio Astrofisico di Torino, 10125 Torino, Italy*
[19]*Department of Physics & Kavli Institute for Cosmological Physics, University of Chicago, Chicago, IL 60637, USA*
[20]*Department of Physics and Astronomy, Rice University, Houston, TX 77005, USA*
[21]*LPNHE, Université Pierre et Marie Curie, Université Paris Diderot, CNRS/IN2P3, Paris 75252, France*
[22]*Physics & Astronomy Department, University of California, Los Angeles, CA 90095, USA*

(Dated: November 27, 2017)

We report the first dark matter search results from XENON1T, a ∼2000-kg-target-mass dual-phase (liquid-gas) xenon time projection chamber in operation at the Laboratori Nazionali del Gran Sasso in Italy and the first ton-scale detector of this kind. The blinded search used 34.2 live days of data acquired between November 2016 and January 2017. Inside the (1042±12) kg fiducial mass and in the [5, 40] $\mathrm{keV_{nr}}$ energy range of interest for WIMP dark matter searches, the electronic recoil background was $(1.93 \pm 0.25) \times 10^{-4}$ events/(kg × day × $\mathrm{keV_{ee}}$), the lowest ever achieved in such a dark matter detector. A profile likelihood analysis shows that the data is consistent with the background-only hypothesis. We derive the most stringent exclusion limits on the spin-independent WIMP-nucleon interaction cross section for WIMP masses above 10 GeV/c^2, with a minimum of 7.7 $\times 10^{-47}$ cm^2 for 35-GeV/c^2 WIMPs at 90% confidence level.

PACS numbers: 95.35.+d, 14.80.Ly, 29.40.-n, 95.55.Vj
Keywords: Dark Matter, Direct Detection, Xenon

Modern cosmology precisely describes observational data from the galactic to cosmological scale with the Λ cold dark matter model [1, 2]. This model requires a nonrelativistic nonbaryonic component of the Universe called *dark matter*, with an energy density of $\Omega_c h^2 = 0.1197 \pm 0.0022$ as measured by Planck [3]. Theories beyond the Standard Model of particle physics (*e.g.*, supersymmetry [4]) often attribute this energy density to weakly interacting massive particles (WIMPs) that may be detectable by underground detectors [5, 6].

The XENON1T experiment is designed primarily for detecting nuclear recoils (NRs) from WIMP-nucleus scattering, continuing the XENON program [7, 8] that employs dual-phase (liquid-gas) xenon time projection chambers (TPCs) [8, 9]. With a total mass of ∼3200 kg of ultra-pure liquid xenon – more than two orders of magnitude larger than the initial detector of the XENON project [7] – XENON1T is the first detector of such scale realized to date. It is located at the Laboratori Nazionali del Gran Sasso (LNGS) in Italy, at an average depth of 3600 m water equivalent. The approximately 97-cm long by 96-cm wide cylindrical TPC encloses (2004 ± 5) kg of liquid xenon (LXe), while another ∼1200 kg provides additional shielding. The TPC is mounted at the center of a 9.6-m diameter, 10-m tall water tank to shield it from ambient radioactivity. An adjacent service building houses the xenon storage, cryogenics plant, data acquisition, and slow control system. The water tank is mounted with 84 photomultiplier tubes (PMTs) as part of a Cherenkov muon veto [10]. The TPC is instrumented with 248 3" Hamamatsu R11410-21 PMTs arranged in two arrays above and below the LXe target [11, 12]. Interactions in the target produce scintillation photons (S1) and ionization electrons. The electrons drift in a (116.7 ± 7.5) V/cm electric field towards the liquid-gas interface at the top of the TPC. They are extracted into the gas by an electric field $E_{\mathrm{gas}} > 10$ kV/cm where, via electroluminescence, they produce a proportional scintillation signal (S2). This charge-to-light amplification allows for the detection of single electrons [13, 14]. The ratio of the S2 to S1 signals is determined by both the ratio of ionization to excitation in the initial interaction and subsequent partial recombination of the ionization, with lower S2/S1 for NR signals than electronic recoils (ERs) from γ and β radiation.

Here we report on 34.2 live days of blinded dark matter search data from the first science run of the experiment. The run started on November 22, 2016, and ended on January 18, 2017, when an earthquake temporarily interrupted detector operations. The detector's temperature, pressure, and liquid level remained stable at (177.08 ± 0.04) K, (1.934 ± 0.001) bar, and (2.5 ± 0.2) mm respectively, where the liquid level was measured above the grounded electrode separating the drift and extraction field regions. While the PMT high voltage remained stable during the run, 27 PMTs were turned off for the dark matter search and 8 were masked in the analysis due to low single-photoelectron (PE) detection efficiency. The PMT response was calibrated periodically using pulsed LED data [15]. The xenon was continuously purified in the gas phase through hot metal getters, leading to an increase in the electron lifetime from 350 to 500 μs, with an average of 452 μs; 673 μs is the drift time over the length of the TPC. Using cryogenic distillation [16], the $^{\mathrm{nat}}$Kr concentration in the LXe was reduced while the TPC was in operation, from (2.60 ± 0.05) ppt [mol/mol] at the beginning of the science run to (0.36 ± 0.06) ppt one month after the end of the science run, as measured by rare-gas mass spectrometry [17] on samples extracted from the detector. The ^{214}Pb event rate was $(0.8 - 1.9) \times 10^{-4}$ events/(kg × day × keV$_{\mathrm{ee}}$) in the low-energy range of interest for WIMP searches, where the bounds are set using *in-situ* α-spectroscopy on ^{218}Po and ^{214}Po. The ^{222}Rn concentration was reduced by ∼20% relative to the equilibrium value using the krypton distillation column in inverse mode [18].

The data acquisition (DAQ) system continuously recorded individual PMT signals. The efficiency for recording single-PE pulses was 92% on average during the science run, and stable to within 2%. A software trigger analyzed the PMT pulses in real-time, allowing for continuous monitoring of the PMTs. The trigger detected S2s larger than 200 PE with 99% efficiency, and saved 1 ms before and after these to ensure small S1s were captured. An analog-sum waveform was separately digitized together with a signal recording when any of the digitizers were inhibited. The average DAQ live time was 92% during the science run.

Physical signals are reconstructed from raw data by finding photon hits in each PMT channel, then clustering and classifying groups of hits as S1 or S2 using the Pax software. For S1s, we require that hits from three or more PMTs occur within 50 ns. To tune the signal reconstruction algorithms and compute their efficiency for detecting NRs – shown in blue in Fig. 1 – we used a Monte Carlo code that reproduces the shapes of S1s and S2s as determined by the interaction physics, light propagation, and detector-electronics chain. This was validated against $^{83\mathrm{m}}$Kr and ^{220}Rn calibration data.

The interaction position is reconstructed from the top-array PMT hit pattern of the S2 (for the transverse position) and the time difference between S1 and S2 (for depth). The S2 transverse position is given by maximizing a likelihood based on an optical simulation of the photons produced in the S2 amplification region. The simulation-derived transverse resolution is ∼2 cm at our S2 analysis threshold of 200 PE (uncorrected). The interaction position is corrected for drift field nonuniformities derived from a finite element simulation, which is validated using $^{83\mathrm{m}}$Kr calibration data. We correct S2s for electron losses during drift, and both S1s and S2s for spatial variations of up to 30% and 15%, respectively,

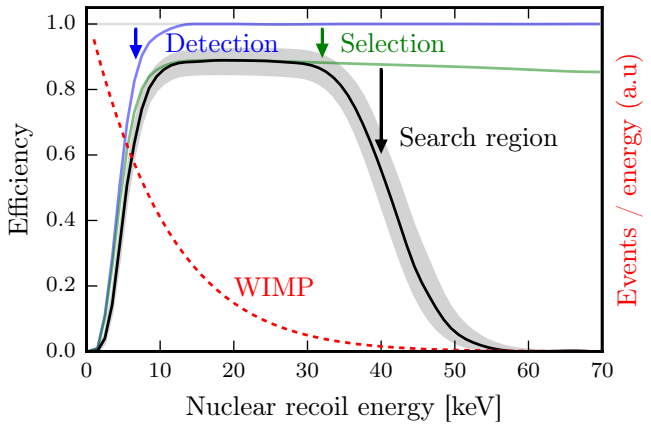

FIG. 1: NR detection efficiency in the fiducial mass at successive analysis stages as a function of recoil energy. At low energy, the detection efficiency (blue) dominates. At 20 keV, the efficiency is 89% primarily due to event selection losses (green). At high energies, the effect of restricting our data to the search region described in the text (black) is dominant. The black line is our final NR efficiency, with uncertainties shown in gray. The NR energy spectrum shape of a 50-GeV/c^2 WIMP (in a.u.) is shown in red for reference.

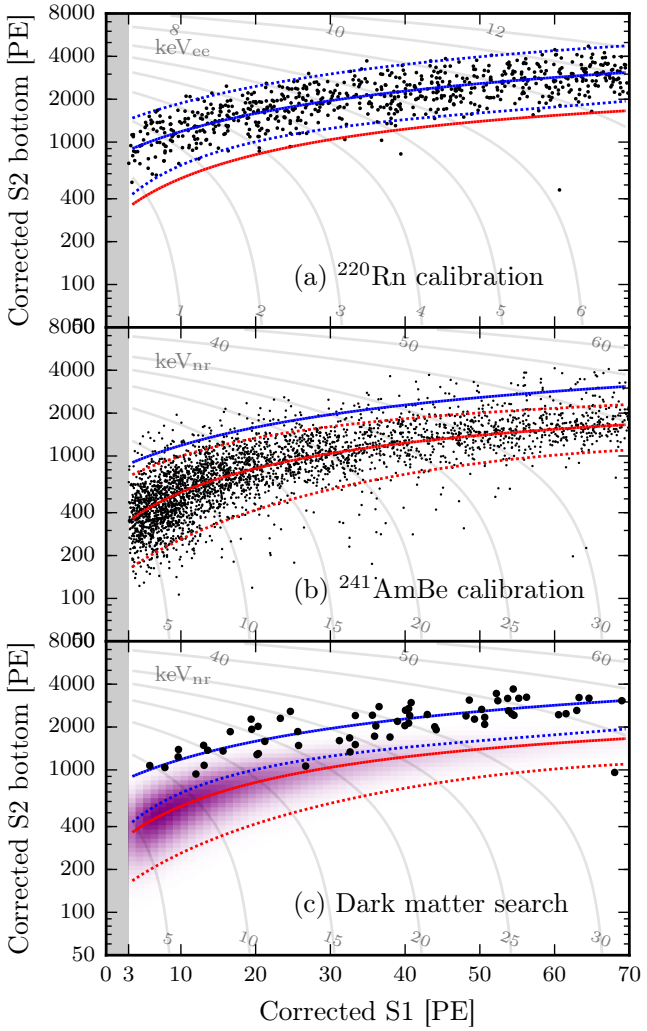

FIG. 2: Observed data in cS2$_b$ vs. cS1 for (a) ^{220}Rn ER calibration, (b) ^{241}AmBe NR calibration, and (c) the 34.2-day dark matter search. Lines indicate the median (solid) and $\pm 2\sigma$ (dotted) quantiles of simulated event distributions (with the simulation fitted to calibration data). Red lines show NR (fitted to ^{241}AmBe) and blue ER (fitted to ^{220}Rn). In (c), the purple distribution indicates the signal model of a 50 GeV/c^2 WIMP. Thin gray lines and labels indicate contours of constant combined energy scale in keV for ER (a) and NR (b, c). Data below cS1 = 3 PE (gray region) is not in our analysis region of interest and shown only for completeness.

inferred from ^{83m}Kr calibration data. These spatial variations are mostly due to geometric light collection effects. The resulting corrected quantities are called cS1 and cS2. As the bottom PMT array has a more homogeneous response to S2 light than the top, this analysis uses cS2$_b$, a quantity similar to cS2 based on the S2 signal seen only by the bottom PMTs.

To calibrate XENON1T, we acquired 3.0 days of data with ^{220}Rn injected into the LXe (for low-energy ERs), 3.3 days with ^{83m}Kr injected into the LXe (for the spatial response) and 16.3 days with an external ^{241}AmBe source (for low-energy NRs). The data from the ^{220}Rn [19] and ^{241}AmBe calibrations is shown in Fig. 2 (a) and (b), respectively. Following the method described in [20] with a W-value of 13.7 eV, we extracted the photon gain $g_1 = (0.144 \pm 0.007)$ PE per photon and electron gain $g_2 = (11.5 \pm 0.8)$ PE (in the bottom array, 2.86 times lower than if both arrays are used) per electron in the fiducial mass by fitting the anti-correlation of cS2$_b$ and cS1 for signals with known energy from ^{83m}Kr (41.5 keV), ^{60}Co from detector materials (1.173 and 1.332 MeV), and from decays of metastable ^{131m}Xe (164 keV) and ^{129m}Xe (236 keV) produced during the ^{241}AmBe calibration. The cS1 and cS2$_b$ yields are stable in time within 0.77% and 1.2% respectively, as determined by ^{83m}Kr calibrations.

WIMPs are expected to induce low-energy single-scatter NRs. Events that are not single scatters in the LXe are removed by several event-selection cuts: (i) a single S2 above 200 PE must be present and any other S2s must be compatible with single electrons from photoionization of impurities or delayed extraction; (ii) an event must not closely follow a high-energy event (*e.g.*, within 8 ms after a 3×10^5 PE S2), which can cause long tails of single electrons; (iii) the S2 signal's duration must be consistent with the depth of the interaction as inferred from the drift time; (iv) the S1 and S2 hit patterns must be consistent with the reconstructed position at which these signals were produced; (v) no more than 300 PE of uncorrelated single electrons and PMT dark counts must appear in the region before the S2. Single scatter NR events within the [5, 40] keV$_{nr}$ energy range

TABLE I: Expected number of events for each background component in the fiducial mass; in the full cS1 $\in [3, 70]$ PE, $cS2_b \in [50, 8000]$ PE search region and in a reference region between the NR median and -2σ quantile in $cS2_b$. Uncertainties <0.005 events are omitted. The ER rate is unconstrained in the likelihood; for illustration, we list the best-fit values to the data in parentheses.

	Full	Reference
Electronic recoils (*ER*)	(62 ± 8)	$(0.26^{+0.11}_{-0.07})$
Radiogenic neutrons (*n*)	0.05 ± 0.01	0.02
CNNS (ν)	0.02	0.01
Accidental coincidences (*acc*)	0.22 ± 0.01	0.06
Wall leakage (*wall*)	0.5 ± 0.3	0.01
Anomalous (*anom*)	$0.10^{+0.10}_{-0.07}$	0.01 ± 0.01
Total background	63 ± 8	$0.36^{+0.11}_{-0.07}$
50 GeV/c^2, 10^{-46}cm^2 WIMP	1.66 ± 0.01	0.82 ± 0.06

pass these selections with >82% probability, as determined using simulated events or control samples derived from calibration, and shown in green in Fig. 1.

The dark matter search uses a cylindrical (1042±12) kg fiducial mass, which was defined before unblinding using the reconstructed spatial distribution of ERs in the dark matter search data and the energy distribution of ERs from ^{220}Rn. We restrict the search to cS1 $\in [3, 70]$ PE and $cS2_b \in [50, 8000]$ PE, which causes little additional loss of WIMP signals, as shown in black in Fig. 1.

Table I lists the six sources of background we consider inside the fiducial mass and inside the search region. For illustration, we also list the expected rate in a reference region between the NR median and -2σ quantile in $cS2_b$ (*i.e.*, between the red lines in Fig. 2c), for which Fig. 3 shows the background model projected onto cS1. This reference region would contain about half of the WIMP candidate events, while excluding 99.6% of the ER background. The WIMP search likelihood analysis uses the full search region. Below we describe each background component in more detail: all event rates are understood to be inside the fiducial mass and the full search region.

First, our background model includes ERs, primarily from β decays of ^{85}Kr and the intrinsic ^{222}Rn-progeny ^{214}Pb, which cause a flat energy spectrum in the energy range of interest [9]. The ER background model is based on a simulation of the detector response. We use a model similar to [21] to convert the energy deposition from ERs into scintillation photons and ionization electrons, which we fit to ^{220}Rn calibration data in (cS1, $cS2_b$) space (Fig. 2a).

The best-fit photon yield and recombination fluctuations are comparable to those of [21]. The model accounts for uncertainties of g_1, g_2, spatial variations of the S1 and S2 light-collection efficiencies, the electron-extraction efficiency, reconstruction and event-selection efficiency, and time dependence of the electron lifetime. The rate of ERs is not constrained in the likelihood analysis, even though we have independent concentration measurements for ^{214}Pb and ^{85}Kr, since the most stringent constraint comes from the search data itself.

Second and third, our background model includes two sources of NRs: radiogenic neutrons contribute (0.05±0.01) events, and coherent neutrino-nucleus scattering (CNNS) ∼0.02 events. Cosmogenically produced neutrons are estimated to contribute $\mathcal{O}(10^{-3})$ events even without muon-veto tagging. The NR background model is built from a detector response simulation that shares the same detector parameters and associated systematic uncertainties as the ER background model above. The main difference is the energy-conversion model, where we use the model and parametrization from NEST [22]. We obtain the XENON1T response to NRs by fitting the ^{241}AmBe calibration data (Fig. 2b) with the light and charge yields from [22] as priors. Our NR response model is therefore constrained by the global fit of external data. It is also used to predict the WIMP signal models in (cS1, $cS2_b$) space. The S1 detection efficiency, which is responsible for our low-energy threshold, is consistent with its prior (0.7σ).

Fourth, accidental coincidences of uncorrelated S1s and S2s are expected to contribute (0.22 ± 0.01) background events. We estimated their rate and (cS1, $cS2_b$) distribution using isolated S1 and S2 signals, which are observed to be at (0.78 ± 0.01) Hz and (3.23 ± 0.03) mHz, respectively, before applying S2-selections. The effect of our event selection on the accidental coincidence rate is included, similar to [23]. Isolated S1s may arise from interactions in regions of the detector with poor charge collection, such as below the cathode, suppressing an associated cS2 signal. Isolated S2s might arise from photoionization at the electrodes, regions with poor light collection, or from delayed extraction [24]. Most accidental events are expected at low cS1 and at lower $cS2_b$ than typical NRs.

Fifth, inward-reconstructed events from near the TPC's PTFE wall are expected to contribute (0.5 ± 0.3) events, with the rate and (cS1, $cS2_b$) spectrum extrapolated from events outside the fiducial mass. Most of these events would appear at unusually low $cS2_b$ due to charge losses near the wall. The inward reconstruction is due to limited position reconstruction resolution, especially limited for small S2s, near the 5 (out of 36) top PMTs in the outermost ring that are unavailable in this analysis.

Sixth and last, we add a small uniform background in the $(cS1, \log cS2_b)$ space for ER events with an anomalous $cS2_b$. Such *anomalous leakage* beyond accidental coincidences has been observed in XENON100 [23], and one such event is seen in the ^{220}Rn calibration data (Fig. 2a). If these were not ^{220}Rn-induced events, their rate would scale with exposure and we would see numerous such events in the WIMP search data. We do not observe

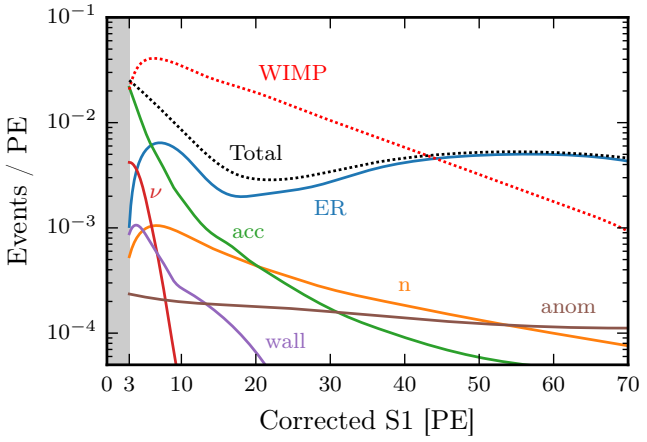

FIG. 3: Background model in the fiducial mass in a reference region between the NR median and -2σ quantile in $cS2_b$, projected onto cS1. Solid lines show that the expected number of events from individual components listed in Table I; the labels match the abbreviations shown in the table. The dotted black line *Total* shows the total background model, the dotted red line *WIMP* shows an $m = 50$ GeV/c^2, $\sigma = 10^{-46}$cm^2 WIMP signal for comparison.

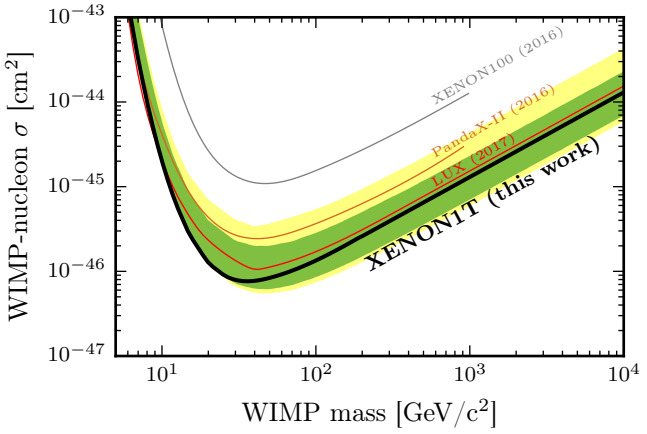

FIG. 4: The spin-independent WIMP-nucleon cross section limits as a function of WIMP mass at 90% confidence level (black) for this run of XENON1T. In green and yellow are the 1- and 2σ sensitivity bands. Results from LUX [27] (red), PandaX-II [28] (brown), and XENON100 [23] (gray) are shown for reference.

this, and therefore assume their rate is proportional to the ER rate, at $0.10^{+0.10}_{-0.07}$ events based on the outliers observed in the ^{220}Rn calibration data. The physical origin of these events is under investigation.

The WIMP search data in a predefined signal box was blinded (99% of ERs were accessible) until the event selection and the fiducial mass boundaries were finalized. We performed a staged unblinding, starting with an exposure of 4 live days distributed evenly throughout the search period. No changes to either the event selection or background types were made at any stage.

A total of 63 events in the 34.2-day dark matter search data pass the selection criteria and are within the $cS1 \in [3, 70]$ PE, $cS2_b \in [50, 8000]$ PE search region used in the likelihood analysis (Fig. 2c). None are within 10 ms of a muon veto trigger. The data is compatible with the ER energy spectrum in [9] and implies an ER rate of $(1.93 \pm 0.25) \times 10^{-4}$ events/(kg $\times$ day $\times$ keV$_{ee}$), compatible with our prediction of $(2.3 \pm 0.2) \times 10^{-4}$ events/(kg $\times$ day $\times$ keV$_{ee}$) [9] updated with the lower Kr concentration measured in the current science run. This is the lowest ER background ever achieved in such a dark matter experiment. A single event far from the bulk distribution was observed at cS1 = 68.0 PE in the initial 4-day unblinding stage. This appears to be a *bona fide* event, though its location in $(cS1, cS2_b)$ (see Fig. 2c) is extreme for all WIMP signal models and background models other than anomalous leakage and accidental coincidence. One event at cS1 = 26.7 PE is at the -2.4σ ER quantile.

For the statistical interpretation of the results, we use an extended unbinned profile likelihood test statistic in (cS1, cS2b). We propagate the uncertainties on the most significant shape parameters (two for NR, two for ER) inferred from the posteriors of the calibration fits to the likelihood. The uncertainties on the rate of each background component mentioned above are also included. The likelihood ratio distribution is approximated by its asymptotic distribution [25]; preliminary toy Monte Carlo checks show the effect on the exclusion significance of this conventional approximation is well within the result's statistical and systematic uncertainties. To account for mismodeling of the ER background, we also calculated the limit using the procedure in [26], which yields a similar result.

The data is consistent with the background-only hypothesis. Fig. 4 shows the 90% confidence level upper limit on the spin-independent WIMP-nucleon cross section, power constrained at the -1σ level of the sensitivity band [29]. The final limit is within 10% of the unconstrained limit for all WIMP masses. For the WIMP energy spectrum we assume a standard isothermal WIMP halo with $v_0 = 220$ km/s, $\rho_{\rm DM} = 0.3$ GeV/cm^3, $v_{\rm esc} = 544$ km/s, and the Helm form factor for the nuclear cross section [30]. No light and charge emission is assumed for WIMPs below 1 keV recoil energy. For all WIMP masses, the background-only hypothesis provides the best fit, with none of the nuisance parameters representing the uncertainties discussed above deviating appreciably from their nominal values. Our results improve upon the previously strongest spin-independent WIMP limit for masses above 10 GeV/c^2. Our strongest exclusion limit is for 35-GeV/c^2 WIMPs, at 7.7×10^{-47}cm^2.

These first results demonstrate that XENON1T has the lowest low-energy background level ever achieved by a dark matter experiment. The sensitivity of XENON1T is the best to date above 20 GeV/c^2, up to twice the

LUX sensitivity above 100 GeV/c^2, and continues to improve with more data. The experiment resumed operation shortly after the January 18, 2017 earthquake and continues to record data.

We gratefully acknowledge support from the National Science Foundation, Swiss National Science Foundation, German Ministry for Education and Research, Max Planck Gesellschaft, Deutsche Forschungsgemeinschaft, Netherlands Organisation for Scientific Research (NWO), NLeSC, Weizmann Institute of Science, I-CORE, Pazy-Vatat, Initial Training Network Invisibles (Marie Curie Actions, PITNGA-2011-289442), Fundacao para a Ciencia e a Tecnologia, Region des Pays de la Loire, Knut and Alice Wallenberg Foundation, Kavli Foundation, and Istituto Nazionale di Fisica Nucleare. Data processing is performed using infrastructures from the Open Science Grid and European Grid Initiative. We are grateful to Laboratori Nazionali del Gran Sasso for hosting and supporting the XENON project.

* jaalbers@nikhef.nl
† Also at Albert Einstein Center for Fundamental Physics, University of Bern, Bern, Switzerland
‡ Wallenberg Academy Fellow
§ Also at Coimbra Engineering Institute, Coimbra, Portugal
¶ guillaume.plante@astro.columbia.edu
** tunnell@uchicago.edu
†† xenon@lngs.infn.it

[1] S. Dodelson, "Modern Cosmology," Amsterdam, Netherlands: Academic Pr. (2003).
[2] E. W. Kolb and M. S. Turner, "The Early Universe," Front. Phys. **69**, 1 (1990).
[3] P.A.R. Ade *et al.* (Planck Collaboration), Astron. Astrophys. **594**, A13 (2016) [arXiv:1502.01589].
[4] G. Jungman, M. Kamionkowski, and K. Griest, Phys. Rep. **267**, 195 (1996).
[5] M. W. Goodman and E. Witten, Phys. Rev. D **31**, 3059 (1985).
[6] T. Marrodán Undagoitia and L. Rauch, J. Phys. G **43**, no. 1, 013001 2016) [arXiv:1509.08767].
[7] E. Aprile *et al.* (XENON Collaboration), Astropart.Phys. **34**, 679 (2011) [arXiv:1001.2834].
[8] E. Aprile *et al.* (XENON100 Collaboration), Astropart. Phys. **35**, 573 (2012) [arXiv:1107.2155].
[9] E. Aprile *et al.* (XENON Collaboration), JCAP **1604**, no. 04, 027 (2016) [arXiv:1512.07501].
[10] E. Aprile *et al.* [XENON1T Collaboration], JINST **9**, 11006 (2014) [arXiv:1406.2374].
[11] E. Aprile *et al.* (XENON Collaboration), Eur. Phys. J. C **75**, no. 11, 546 (2015) [arXiv:1503.07698].
[12] P. Barrow *et al.* JINST **12**, no. 01, P01024 (2017) [arXiv:1609.01654].
[13] B. Edwards *et al.* (ZEPLIN-II Collaboration), Astropart. Phys. **30**, 54 (2008) [arXiv:0708.0768].
[14] E. Aprile *et al.* (XENON100 Collaboration), J. Phys. G **41**, 035201 (2014) [arXiv:1311.1088].
[15] R. Saldanha, *et al.* (2016) [arXiv:1602.03150].
[16] E. Aprile *et al.* (XENON Collaboration), Eur. Phys. J. C **77**, 275 (2017) [arXiv:1612.04284].
[17] S. Lindemann, H. Simgen, Eur. Phys. J. C **74**, 2746 (2014) [arXiv:1308.4806].
[18] E. Aprile *et al.* (XENON Collaboration), (2017) [arXiv:1702.06942].
[19] E. Aprile *et al.* (XENON Collaboration), Phys. Rev. D **95**, 72008 (2017) [arXiv:1611.03585].
[20] C.E. Dahl, Ph.D Thesis, Princeton University (2009).
[21] D. S. Akerib *et al.* (LUX Collaboration), Phys. Rev. D **93**, no. 7, 72009 (2016) [arXiv:1512.03133].
[22] B. Lenardo *et al.*, IEEE Transactions on Nuclear Science **62**, no. 06, 3387 (2015) [arXiv:1412.4417].
[23] E. Aprile *et al.* (XENON Collaboration), Phys. Rev. D **94**, 122001 (2016) [arXiv:1609.06154].
[24] P. Sorensen. (2017) [arXiv:1702.04805].
[25] G. Cowan, K. Cranmer, E. Gross and O. Vitells, Eur. Phys. J. C **71**, 1554 (2011) Erratum: [Eur. Phys. J. C **73**, 2501 (2013)] [arXiv:1007.1727].
[26] N. Priel, L. Rauch, H. Landsman, A. Manfredini, and R. Budnik, J. Cosmol. Astropart. Phys. **5** 13 (2017) [arXiv:1610.02643].
[27] D. S. Akerib *et al.* (LUX Collaboration), Phys. Rev. Lett. **118**, no. 2, 021303 (2017) [arXiv:1608.07648].
[28] A. Tan *et al.* [PandaX-II Collaboration], Phys. Rev. Lett. **117**, no. 12, 121303 (2016) [arXiv:1607.07400].
[29] G. Cowan, K. Cranmer, E. Gross and O. Vitells, (2011) [arXiv:1105.3166].
[30] J. Lewin and P. Smith, Astropart. Phys. **6** 87 (1996).